THE UNIVERSITY OF CHICAGO

CHARACTERIZING METABOLIC ADAPTATIONS OF PANCREATIC CANCER TO TUMOR NUTRIENT STRESS

A DISSERTATION SUBMITTED TO

THE FACULTY OF THE DIVISION OF THE BIOLOGICAL SCIENCES

AND THE PRITZKER SCHOOL OF MEDICINE

IN CANDIDACY FOR THE DEGREE OF

DOCTOR OF PHILOSOPHY

COMMITTEE ON CANCER BIOLOGY

BY

JUAN JOSÉ ÁPIZ SAAB

CHICAGO, ILLINOIS

DECEMBER 2023

For my family

Poco a poco vamos caminando, poco a poco iremos llegando

TABLE OF CONTENT

LIST OF FIGURES

Acknowledgments

It's hard to write acknowledgments for five years of your life. Especially when, prior to these five years, many people were also instrumental in getting you here. So, although I can't cover everybody, I'll start from the present and try to work my way back.

I want to first thank my thesis committee. Daria, who joined my qualifying exam from Germany in the middle of a pandemic, Kay, who made herself accessible to listen to my questions and concerns even before I joined the program, and Lev, who would not conform to the sporadic committee meetings and would catch up with me through lengthy conversations whenever we bumped into each other. These were of course only some memorable examples of your support, and I'm very grateful for the time you put into advising and supporting me.

I also want to thank every member of the Muir lab, which cumulatively has been deceivingly large, so I apologize for not mentioning all by name, but I truly am thankful to everybody. Thanks, Lindsey, for being my partner in crime while we tried to do so much from scratch. Thanks, James and Guillaume for all your advice, scientific and not. Both of you are extremely wise beyond your years and talking things out with you made me a better scientist and person. Thanks to Rio, Violet, Moses, Lyndon, Colin, Patrick, Grace, Chufan, and everybody else I had the pleasure to work and exchange ideas, frustrations, and great moments with. I'm sure that each one of you will accomplish great things and I can't wait to be your biggest cheerleader.

Alex, thanks so much for being my mentor, a colleague, an administrator, a cheerleader, a leader, and more. With the many hats you wore interchangeably and simultaneously, I'm surprised I went bald before you did. Thanks for holding me and my science to the highest standard while also being your characteristic patient and understanding self. I'm glad we crossed paths at the

University of Chicago, and I can't wait to see what amazing things come out of Alexander Muir's Tumor Microenvironment Observatory.

Thanks to everybody who helped me move forward day by day. To Jerry, the security guard from 2017-18 at the Apostolic Church. You gave me my first winter jacket and wouldn't take any money for it when I told you I was saving for a trip to Puerto Rico. I never got a chance to repay you but know that I haven't gotten another winter jacket since and will never forget about you. Jay and JT, you adopted me and Melissa as part of your family despite having enough family of your own. I'm forever grateful and this degree is also thanks to you. To Angeliz, Carlos, Suzy, Steven, Margo, Liam, Lizeth, and all other friends who gave me advice and an ear to vent when I needed it most, I also owe this success to you. Thanks to professors Michael Rubin, Pablo Vivas, and Waldo Torres. You all believed in me, and that made me believe in myself. I'm sorry to the many people that I didn't mention here but know that no push was too soft to go unnoticed.

Mamá y papá, no voy a intentar usar muchas líneas para agradecerles por todo lo que han hecho porque, aunque esto no hubiese sido posible sin ustedes, les debo tanto además de este doctorado que prefiero dedicarme a demostrarles mi agradecimiento de tantas otras maneras. Ustedes han sido mi roca, mi inspiración y mi luz. Los amo. Susa y Berna, quiero que sepan que son la inspiración más grande para mí y siempre aspiro a ser más como ustedes de tantas maneras. Abu, Leo y el resto de mi familia, gracias por joderse trabajando mientras yo estoy aquí. Esto tampoco hubiese sido posible sin ustedes. Melissa, sabes que este doctorado es tan tuyo como mío y ni en mil años podre repagarte por estos últimos cinco. Té amo y te admiro.

Finally, thanks to those who I will never get to thank in person again. I'm still conflicted about whether putting your names here in any way trivializes how grateful I am and how meaningful you are to me, but I'll take any chance I can get to say thank you. Tío José Antonio, I

love you and I'm sorry we never spoke all those years you were struggling with pancreatic cancer. I still remember the joy I would get from your visits in Maracay and since then, I've learned how much more present you were in my life than I could remember. Prof. Edwin Vázquez de Jesus, you showed me that I can be a scientist and an activist and that I don't have to compromise my ideals to do good science and work on what I love. Especially when I'm not sure about what I'm trying to do, I always remember that conversation we had about science, Puerto Rico, and life, when I realized that I had a long journey ahead and that I would be ok. This goes to you.

ABSTRACT

Nutrient stress in the tumor microenvironment (TME) requires cancer cells to adopt adaptive metabolic programs for survival and proliferation. Therefore, knowledge of microenvironmental nutrient levels and how cancer cells cope with such nutrition is critical to understand the metabolism underpinning cancer cell biology. Characterizing the metabolic adaptations of cancer cells under the nutrient constraints of the TME can lead to the discovery of novel targetable tumor liabilities. However, our ability to study such adaptations has been precluded by our limited understanding of the metabolic make-up of the TME.

Tumor interstitial fluid (TIF) is the local perfusate of the TME that carries metabolites, electrolytes, and soluble macromolecules to tumor resident cells. Previously, we performed quantitative metabolomics of the TIF of murine pancreatic ductal adenocarcinoma (PDAC) tumors to comprehensively characterize nutrient availability in the PDAC TME. In this dissertation, we develop Tumor Interstitial Fluid Medium (TIFM), a cell culture medium that contains nutrient levels representative of the PDAC microenvironment, enabling us to study PDAC metabolism ex vivo under physiological nutrient conditions. We show that PDAC cells cultured in TIFM adopt a cellular state closer to that of PDAC cells present in tumors compared to standard culture models.

Further, using the TIFM model, we found arginine biosynthesis is active in PDAC and allows PDAC cells to maintain levels of this amino acid despite microenvironmental arginine depletion. We also show that myeloid-derived arginase activity is largely responsible for the low levels of arginine in PDAC tumors. Altogether, these data indicate that nutrient availability in tumors is an important determinant of cancer cell metabolism and behavior, and cell culture models that incorporate physiological nutrient availability have improved fidelity to *in vivo* systems and enable the discovery of novel cancer metabolic phenotypes.

CHAPTER 1

INTRODUCTION

1.1 THE TUMOR MICROENVIRONMENT'S ROLE IN CELL STATE AND CANCER DISEASE PROGRESSION

When revising the hallmarks of cancer in 2011, Hanahan and Weinberg identified (1) deregulating metabolism and (2) cancer cells' interactions within the tumor microenvironment (TME) as key features that underpin disease progression in most tumors [1,2]. Subsequent research has demonstrated that these are not separate hallmarks of cancer, but instead are deeply interconnected, and that the influence of the TME on cellular metabolism is an important determinant of tumor growth, survival, and metastatic potential [3–5].

Altered cellular metabolism is common in cancers [6] and enables many pathological features of tumors [4,7]. This has led to substantial interest in determining the metabolic properties of tumor cells, both for understanding the basic biochemistry underlying these diseases and identifying novel therapeutic targets. Recent work has led to the understanding that tumor metabolic phenotypes are driven both by cancer cell-intrinsic factors, such as oncogenic lesions and cellular epigenetic identity [8,9] , and by cell-extrinsic factors in the TME [10–13]. While we have a relatively extensive understanding of cell-intrinsic regulation of cancer metabolism, we know comparatively little about TME regulation of cancer metabolism and the contributions of such TME-driven metabolic phenotypes to tumor biology.

The TME consists of 3 components: tumor resident cells, the extracellular matrix, and the interstitial space, which is filled with tumor interstitial fluid (TIF). TIF is the local perfusate of tumors and baths all cells in the tumor parenchyma with nutrients, ions, and soluble

macromolecules[14]. Thus, TIF acts as the interface between cells in a tumor and the circulation (Figure 1.1). Our increasing understanding of the importance of the TME in cancer biology has led to the recent development of technologies to interrogate the composition of each TME component and how these regulate tumor biology. For example, recent developments in single cell analysis techniques have enabled comprehensive analysis of the cellular composition of the TME[15]. New bioinformatic methods have also led to discoveries of how cells in the TME communicate, providing insight into how the cellular composition of the TME regulates cell state and function[16]. New proteomics techniques have been developed to study extracellular matrix composition in tumors[17] and how matrix composition influences the biology of cancer and stromal cells[18–20]. Similarly, new approaches to determine TIF composition and probe TIF-cell interactions have been recently developed to understand how the TIF compartment of the TME regulates cancer biology.

Nutrient availability is a key cell-extrinsic factor that influences cellular metabolism [13,21,22]. Many solid tumors have abnormal vasculature that limits tumor perfusion [14,23–25], which leads to abnormal nutrient availability in the TME [26–28]. Thus, perturbed nutrient availability in the TME has been postulated to be a critical driver of cancer metabolic phenotypes [29,30]. A good example of this is pancreatic ductal adenocarcinoma (PDAC). PDAC tumors are characterized by abundant fibrotic stroma and abnormal vasculature, with only around 30% of blood vessels actively transporting blood[24,31]. This pathology limits nutrient delivery and removal of waste products from cells within the tumor. This, in combination with the dynamic metabolic interplay discussed above, results in a microenvironment with altered nutrient availability, to which the PDAC cells need to adapt. Characterizing how cancer cells adapt to the abnormal nutrient availability in the tumor microenvironment represents a good opportunity to

identify metabolic liabilities that cells in well-perfused normal tissues do not need to rely on, and thus could provide a wider therapeutic window. Indeed, there has been a lot of interest in targeting PDAC metabolic adaptations[32]. However, the precise metabolic changes driven by TME-nutrient cues are largely unknown due to a dearth of information on the nutrient milieu of tumors and a lack of experimentally tractable model systems to study cellular metabolism under such constraints [33,34].

1.2 TIF REGULATION OF CANCER CELL METABOLISM AND BIOLOGY

Techniques to sample interstitial fluid from tissues and tumors have been available for decades and have been critical for studying tissue physiology[14,35]. These techniques have been used to isolate TIF from cancers to study their composition, including pioneering studies in 1964 by Gullino and colleagues, who reported the glucose, lactate, sterol, and amino acid concentrations in TIF from rodent models of cancer[26]. However, many classical techniques for TIF sampling require complex equipment, bespoke materials, and expertise in human or animal experimentation[36]. These experimental difficulties have limited access to TIF samples. However, Wiig and colleagues recently developed a simple method requiring no specialized equipment or materials to isolate TIF from rapidly resected tumors using centrifugal force[37–39] (Figure 1.1). Extensive tracer analysis confirmed that fluid isolated by this approach is *bone fide* TIF and not contaminated with intracellular fluid[37–39]. Thus, recent advances in TIF extraction techniques have enabled non-specialist research teams to access TIF from animal and human cancers. This new TIF isolation method, combined with advances in bioanalytical techniques, has significantly improved our knowledge of TIF composition. Below we will discuss studies that have

used these novel approaches to isolate TIF and gain new insight into the mechanisms by which the TME influences the biology of different tumor resident cells.

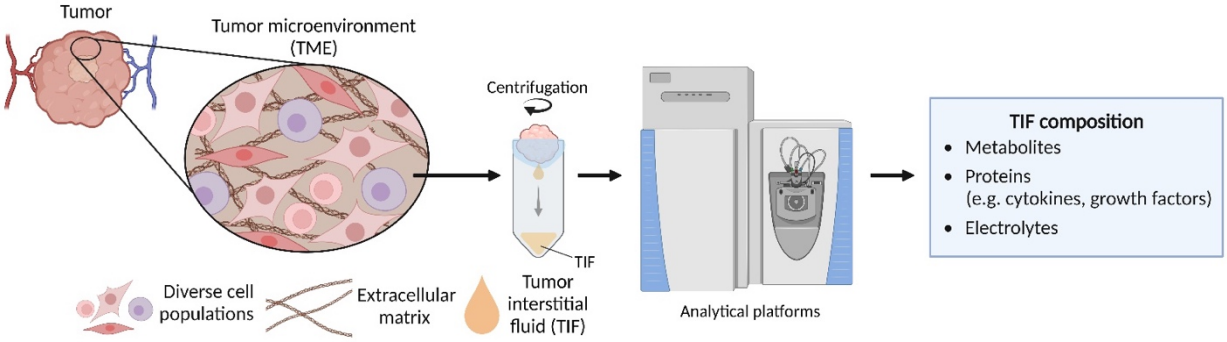

Figure 1.1. Interstitial fluid is the liquid phase of the tumor microenvironment. The tumor microenvironment is comprised of cellular, extracellular matrix, and interstitial fluid components. The interstitial fluid is the perfusate of solid tumors and directly contacts cells residing in the tumor parenchyma carrying metabolites, ions, and soluble macromolecules to these cells. Recently, simple and robust techniques have been developed to isolate interstitial fluid from resected tumors by centrifugation, providing ready access to the interstitial compartment of the TME. Coupled with advances in bioanalytical chemistry enabling high-throughput molecular characterization of small-volume biofluid samples, these advances in tumor interstitial fluid isolation have led to an increasing understanding of the metabolic, proteomic, and ionic composition of the tumor microenvironment.

The abnormal vasculature of many solid tumors has led to the longstanding hypothesis that the TME is nutrient-starved. Such starvation could alter the metabolism of cancer cells by forcing them to rely on compensatory metabolic adaptations to deal with such nutrient stresses[30]. Recent TIF analysis supports this hypothesis and has led to the identification of such metabolic adaptations to TME nutrient stress. For example, our team performed quantitative metabolite profiling of murine pancreatic TIF, allowing us to measure the concentration of ~120 nutrients in the TME of pancreatic tumors[40]. We then built a custom cell culture formulation, enabling us to grow pancreatic cancer cells with TIF levels of nutrients and ask how their biology is affected as the cells adapt to TME nutrient conditions[41]. Using these tools, we found that pancreatic cancer cell biology is heavily influenced by TIF nutrient levels, particularly amino acid stress caused by low

arginine levels in TIF. We found that cancer cells utilize compensatory *de novo* synthesis to cope with the starvation of arginine in pancreatic cancer TIF[41]. Lee and colleagues similarly observed that arginine is deprived in pancreatic cancer TIF. This led them to identify a novel non-arginine-requiring polyamine synthesis pathway that pancreatic cancers require to maintain polyamine homeostasis despite arginine starvation[42]. Thus, analysis of TIF nutrient levels can provide new insight into the metabolic constraints that regulate cancer cell metabolism in the TME.

In addition to TIF analysis providing insight into the metabolism and biology of cancer cells in primary tumors, recent studies have used interstitial fluid analysis of tissues to which tumors will metastasize to understand the metabolic adaptations cancer cells use during metastatic colonization. For example, analysis of brain interstitial fluid revealed low levels of amino acids, including serine, and low levels of lipids in the brain microenvironment[43,44]. Subsequently, studies have found that breast cancer cells metastasizing to the brain require compensatory metabolic adaptations to cope with these limitations. Breast cancer cells metastasizing to the brain increase synthesis of both serine and lipids, which they require to grow in the brain[43,44]. In another example of unique tissue microenvironments impacting the metabolism of metastasizing cancer cells, low levels of arginine and glutamine, but higher levels of pyruvate and palmitate were observed in lung interstitial fluid[45–47]. This unique metabolic composition of the lung interstitial fluid also appears to drive shifts in the metabolism of cancer cells as they colonize the lung. For example, renal carcinomas metastasizing to the lung were found to upregulate arginine synthesis to cope with arginine limitation in the lung, and inhibition of arginine synthesis reduced the ability of renal carcinomas to colonize the lung[45]. Breast cancer cells colonizing the lung increase their use of pyruvate carboxylation for TCA cycle anaplerosis to compensate for lowered glutamine availability[46] and use fatty acid oxidation of the abundant microenvironmental

palmitate to colonize the lung[47]. Thus, interstitial fluid analysis of organs to which tumors will metastasize can identify how cancer cell metabolism and biology shift to enable metastatic disease progression.

1.3 TIF REGULATION OF ANTI-TUMOR IMMUNITY

The TME of many cancers is immunosuppressive and potently inhibits effector T cells while promoting the functions of suppressive cells[48,49]. TIF analysis has provided insight into how the TME regulates immune cells in this way. Several groups have analyzed the metabolite composition of melanoma TIF. These findings indicate that key metabolic substrates like glucose are depleted in the TME of melanoma[27,50]. This shift in nutrient availability has been shown to contribute to altered T cell function in the TME. For example, low glucose levels have been shown to impair T cell signaling[27] and metabolism[27,50], which causes T cell dysfunction in the TME. However, care must be taken with extending these findings from melanomas to other tumor types, as measurements of TIF glucose in different cancer types suggest glucose deprivation may not be a universal feature of all TMEs[40,51,52]. Nevertheless, TIF analysis has led to the discovery that metabolic substrate limitation is an immunosuppressive regulator of T cell biology in certain tumor types. Identifying nutrient limitation as a critical node of tumor immunosuppression could lead to new methods to prevent pathological TME reprogramming of the immune system, such as treatments enabling tumor infiltrating T cells to utilize nutrient sources such as lipids, which are not limited in the TME[50].

Nutrient limitation is not the only feature of TIF that regulates immune cell metabolism and biology. Metabolomic analysis of melanoma TIF uncovered high levels of lactate[53], many classes of lipids[50,54], and nucleotides[28] in the TME. Clinical chemistry analysis of melanoma TIF also indicates high potassium levels in the TME[55]. These enriched metabolites and

electrolytes are also potent regulators of immune cell function. For example, lactate has been found to influence the functions of different T cell classes. Lactate suppresses the proliferation of $CD8^+$ T cells[56], but high lactate levels stabilize and promote the suppressive function of Treg cells[53]. In another example, T cells exposed to high levels of oxidized lipids in TIF become dysfunctional upon taking up these lipids, which causes intracellular lipid peroxidation and triggers T cell dysfunction[54]. Lastly, high potassium levels have also been found to suppress T cell metabolism by impairing nutrient transport mechanisms in T cells[57], suppressing their functions[55]. Not all metabolites increased in TIF suppress immune cell function. For example, uridine diphosphate and guanosine diphosphate, two nucleotides elevated in melanoma TIF, were found to increase the effector functions of stimulated T cells[28]. Further increasing TIF levels of these nucleotides could improve tumor control by the immune system[28]. Thus, TIF analysis has determined that substrate limitation is not the only metabolic regulator of immune cell function in the TME. Instead, metabolites that accumulate in TIF are also potent regulators of immune cell metabolism and function in the TME.

1.4 THE CONTRIBUTION OF MY WORK

With advances in our ability to study cell metabolism and the TME, we have come to appreciate the key role of cell-extrinsic factors in regulating tumor metabolism [11,12,21]. In Chapter 3, to determine how TME nutrients influence cancer cells, we performed a transcriptomic analysis of murine PDAC cells growing in TIFM, standard culture, and orthotopic tumors. Through this analysis, we found that many transcriptional features of PDAC cells growing *in vivo* are better recapitulated in TIFM culture compared to standard culture models. This suggests that altered nutrient availability is a major regulator of the cancer cell state in the TME. Thus, *ex vivo* models incorporating physiological nutrition could improve the fidelity of cell culture models of

cancer [58]. A major metabolic signature we found in PDAC cells in TIFM and *in vivo* was activation of the amino acid starvation transcriptional signature, including increased expression of the *de novo* arginine synthesis pathway. In Chapters 4 and 5, we show that the *de novo* arginine synthesis pathway enables PDAC cells in TIFM and in tumors to acquire the arginine needed for amino acid homeostasis despite TME arginine starvation, and that PDAC cells are readily adaptable to perturbations in arginine homeostasis. Further, in Chapter 6 we show that myeloid-driven arginase activity is responsible for arginine deprivation in the PDAC TME. Collectively, this work identifies TME nutrient availability as a key regulator of the *in vivo* cancer cell phenotype and demonstrates that analysis of cancer cells under physiological nutrient conditions can identify *bone fide* metabolic features of tumors, such as *de novo* arginine synthesis in PDAC.

CHAPTER 2

MATERIALS AND METHODS

2.1 Formulation of Tumor Interstitial Fluid Media

TIFM is composed of 115 nutrients at levels that match the average measurements in the IF of murine *Kras*$^{LSL\text{-}G12D/+}$*; Trp53*$^{fl/fl}$ *Pdx1*^{Cre} PDAC tumors [40]. The medium is composed of 10 pools of metabolites each of which is formulated by compounding dry powders of nutrients at appropriate ratios using a knife mill homogenizer. To generate the complete medium, the 10 metabolite mixture powders are added together and reconstituted in water with 10% dialyzed fetal bovine serum (FBS) to provide essential lipids, proteins and growth factors. The electrolytes provided in pool 3 are adjusted so that the electrolyte balance will be the same as RPMI-1640 medium, correcting for the sodium chloride in the FBS and counter ions of the various metabolites used to make TIFM. We performed quantitative LC-MS metabolite profiling (see **Quantification of metabolite levels in cell culture media**) to ensure concentrations of nutrients in TIFM are reproducibly close to the formulated concentration (Fig. 1B).

2.2 Quantification of metabolite levels in cell culture media

For quantification of metabolites in cell culture media, quantitative metabolite profiling of fluid samples was performed on tissue culture media samples as previously described [40]. Briefly, chemical standard libraries of 149 metabolites in seven pooled libraries were prepared and serially diluted in HPLC grade water from in a dilution series from 5mM to 1µM to generate 'external standard pools', which are used for calibration of isotopically labeled internal standards and to quantitate concentrations of metabolites where internal standards were not available.

We then extracted metabolites from 5µL of either cell culture media samples or external standard pool dilutions using 45µL of a 75:25:0.1 HPLC grade acetonitrile:methanol:formic acid extraction mix with the following labelled stable isotope internal standards:

- ^{13}C labeled yeast extract (Cambridge Isotope Laboratory, Andover, MA, ISO1)
- $^{2}H_9$ choline (Cambridge Isotope Laboratory,Andover, MA, DLM-549)
- $^{13}C_4$ 3-hydroxybutyrate (Cambridge Isotope Laboratory, Andover, MA, CLM-3853)
- $^{13}C_6{}^{15}N_2$ cystine (Cambridge Isotope Laboratory, Andover, MA, CNLM4244)
- $^{13}C_3$ lactate (Sigma Aldrich, Darmstadt, Germany, 485926)
- $^{13}C_6$ glucose (Cambridge Isotope Laboratory, Andover, MA, CLM-1396)
- $^{13}C_3$ serine (Cam-bridge Isotope Laboratory, Andover, MA, CLM-1574)
- $^{13}C_2$ glycine (Cambridge Isotope Laboratory, Andover, MA, CLM-1017)
- $^{13}C_5$ hypoxanthine (Cambridge Isotope Laboratory, Andover, MA, CLM8042)
- $^{13}C_2$15N taurine (Cambridge Isotope Laboratory, Andover, MA, CNLM-10253)
- $^{13}C_3$ glycerol (Cambridge Isotope Laboratory, Andover, MA, CLM-1510)
- $^{2}H_3$ creatinine (Cambridge Isotope Laboratory, Andover, MA, DLM-3653)

Samples in extraction mix were vortexed for 10 min at 4°C and centrifugated at 15,000x rpm for 10 min at 4°C to pellet insoluble material. 20µL of the soluble polar metabolite supernatant was moved to sample vials for analysis by LC-MS as previously described [40,59].

Once LC-MS analysis was performed, XCalibur 2.2 software (Thermo Fisher Scientific) was used for metabolite identification. External standard libraries were used to confirm the m/z and retention time for each metabolite. For quantitative analysis, when internal standards were

available, external standard libraries were used to quantitate concentrations of isotopically labeled internal standards in the extraction mix. Once internal standard concentrations were obtained, the peak areas of the unlabeled metabolites in the media samples were compared with the peak area of the quantified internal standard to determine the metabolite concentration in the media sample.

For metabolites for which an internal standard was not present in the extraction mix, external standard libraries were used to perform analysis of relevant metabolite concentrations. Briefly, the peak area of the metabolite was normalized to the peak area of an isotopically labeled internal standard with similar elution time, both in media samples and external standard library dilutions. Using the external standard library dilutions, we created a standard curve based on the linear relationship of the normalized peak area and the concentration of the metabolite, excluding those metabolites with an $r^2 < 0.95$. This standard curve was then used to interpolate the concentration of the metabolite in the media sample.

2.3 Cell Isolation from tumors

Murine cancer cell lines were derived from tumor bearing C57Bl6J *Kras*$^{LSL\text{-}G12D/+}$; *Trp53*$^{fl/fl}$;*Rosa26* $^{tm1(EYFP)Cos}$; *Pdx1*^{Cre} mice to allow for fluorescent lineage tracing and isolation of cancer cells [60]. To isolate cancer cells from these tumors, the tumors were chopped finely and digested with 30mg/mL dipase II (Roche 28405100), 10mg/mL collagenase I (Worthington LS004194) and 10mg/mL DNase by constant rotation at 37C for 30 min. Digestion was quenched with 0.5M Ethylenediaminetetraacetic acid (EDTA) and cells were passed through a 70μM filter and rinsed with PBS before platting in RPMI-1640 (Corning 50–020-PC) or TIFM. YFP+ Cancer cells from each tumor were sorted twice on a BD FACSAria II Cell Sorter.

2.4 Cell lines and cell culture

Use of cancer cell lines was approved by the Institutional Biosafety Committee (IBC no. 1560). All cell lines were tested quarterly for mycoplasma using the MycoAlert Mycoplasma Detection Kit (Lonza LT07-318). All cells were cultured in Heracell vios 160i incubators (Thermofisher) at 37°C and 5% CO2. Cell lines were routinely maintained in RPMI-1640 or TIFM supplemented with 10% diaFBS (Gibco, #26400-044, Lot#2244935P).

All cell culture was performed in static culture conditions. TIFM contains substantially lower levels of nutrients than most standard media formulations. Therefore, to ensure that there was not nutrient deprivation in static cultures, the following modifications to standard tissue culture practices were made. Cells were cultured in larger volumes of media (8mL/35mm diameter well) to prevent depletion of nutrients during the culture. Additionally, media were replaced every 24 hrs. We routinely measured the concentration of the most rapidly consumed nutrient, glucose, using a GlucCell glucometer [61] to ensure that cultures used in experiments did not experience a greater than 30% drop in glucose availability, which is within the range of mouse PDAC TIF glucose concentration measurements [40]. Lastly, passaging TIFM maintained cells using standard trypsin (0.025%)/EDTA solution to detach cells leads to loss of viability upon replating of cells. Therefore, cells were detached with a 1:1 mixture of 0.5% trypsin-EDTA (Thermofisher) and serum free RPMI-1640 media (Thermofisher). This allowed routine passaging and plating of cells with less loss of viability. These modifications were followed for both TIFM and RPMI cultured cells.

2.5 Determining cellular proliferation rate

Quantification of cellular proliferation rate was performed by sulforhodamine B (SRB) assay as described [62]. Briefly, 10,000-15,000 cells were plated in 12-well plates in triplicates for each condition and allowed to attach overnight. After attachment, one set of triplicate wells was fixed by adding 10% trichloroacetic acid (TCA) to the media and incubating plates in 4°C to provide an 'initial day' value. Media was changed on remaining cultures and were allowed to grow for the indicated number of days. At the end of the growth period, cells were fixed by adding 10% trichloroacetic acid (TCA) to the media and incubating plates in 4°C for at least one hour. All wells were washed with deionized water, air-dried at room temperature, and stained with SRB in 1% acetic acid for 30 min. After, cells were washed with 1% acetic acid three times and dried at 30°C for 15 minutes. SRB dye was solubilized with 10mM Tris pH 10.5 by gentle horizontal shaking for 5 min. Absorbance (abs) was measured at 510 nm in a clear 96-well plate using a BioTek Cytation 1 Cell Imaging Multi-Mode Reader. After all measurements were normalized to an averaged blank measurement (wells without cells but with media), growth rate was calculated using the following equation:

$$\text{Doublings/day} = \log_2(\text{Final Day Abs}_{510}/\text{Initial Day Abs}_{510}) \,/\, \text{number of days elapsed in culture period}$$

2.6 Consumption/Release (Co/Re) analysis

Cellular consumption and metabolite release were measured according to previous publications [63–65]. 100,000-150,000 cells were seeded in 2mL of culture medium in six-well

plates with 3 technical replicates per condition per time point and allowed to attach overnight. The following day (day 1), cells were washed twice with 2mL PBS. They were then given 2mL of media, either TIFM or RPMI. An unspent media sample was also collected at this time and stored at -80 °C. Cell number on day 1 was measured using a Vi-CELL XR Cell Viability Analyzer (Beckman Coulter). 24h later (day 2), 1mL of spent media from cells was collected, centrifuged and stored at -80 °C. Cell number was counted again. Quantification of metabolite levels in unspent (day 1) and day 2 (conditioned media) cell culture media samples was performed as described in **Quantification of metabolite levels in cell culture media**.

To calculate Co/Re rates of a given metabolite, cell numbers on day 1 and day 2 were used to fit an exponential growth function, which integrated yielded the number of (cell·days). Changes in nutrient concentration in cultures were then normalized to this integrated growth curve to yield metabolite Co/Re per cell per unit of time (pmol/cell/day). Standard error mean was calculated for quantified metabolite levels and for the integrated growth curves. These standard error measurements were then used to calculate the propagated error of the Co/Re measurements.

2.7 Experimental set up for consumption of arginine by GC-MS analysis

Cells were plated as described for consumption/release (Co/Re) analysis as described in **Consumption/Release (Co/Re) analysis**. The following day, cells were changed into either TIFM or TIFM without citrulline and ornithine. Both media were supplemented with 20μM extracellular arginine. Day 1 and day 2 media samples were collected and cell numbers were measured as in **Consumption/Release (Co/Re) analysis**.

10μL of each media sample were mixed 10μL of water containing $^{13}C_6$,$^{15}N_4$ arginine at 20μM and 600μL cold HPLC grade methanol. The solution was then vortexed for 10 min, and

centrifuged at 21,000xg for 10 min. Finally, 450µL of each extract was aliquoted, dried under nitrogen gas and stored at -80°C before further analysis. Sample derivatization GC-MS was then used to measure the arginine concentration in each media sample as described below in **GC-MS analysis of arginine**.

2.8 RNA extraction, library preparation and transcriptomic analyses

2.8.1 Isolation of cultured and tumor cancer cell samples

mPDAC3-TIFM cells were plated at 200,000 (TIFM) to 350,000 (RPMI) cells per 6cm plate in triplicate cultures. RNA was extracted from cells 24 hrs later when the cells were proliferating exponentially. The cells were trypsinized and isolated by fluorescence activated cell sorting (FACS) for RNA extraction. For the *in vivo*, condition cells were isolated by FACS from end stage orthotopic mPDAC3-TIFM tumors, as described in **Cell isolation from tumors**.

2.8.2 RNA extraction

Cells from all conditions were sorted by FACS prior to RNA extraction to eliminate the FACS sorting process as a confounder between cultured mPDAC3-TIFM cells and those isolated from orthotopic tumors. For FACS sorting, cells were stained with DAPI (750 ng/mL) to separate dead/dying cells from live cells, and live YFP+/DAPI- cells were sorted with a BD FACSAria II Cell Sorter with a 100µm nozzle directly into Qiagen RLT RNA extraction buffer. The ratio of RNA extraction buffer to sorted cellular volume was kept at 100µL of sorted sample per 350µL of RNA extraction buffer. Total messenger RNA (mRNA) was extracted using the RNeasy Micro

Kit (Qiagen #74004) and RNA quality and quantity was assessed using the 2100 Bioanalyzer System (Agilent).

2.8.3 Library preparation and sequencing

Strand-specific RNA-SEQ libraries were prepared using an TruSEQ mRNA RNA-SEQ library protocol (Illumina). Library quality and quantity was assessed using the Agilent bio-analyzer and libraries were sequenced using an Illumina NovaSEQ6000.

2.8.4 Transcriptomic analyses

Data processing and analysis was done using the R-based Galaxy platform (https://usegalaxy.org/) [66]. Quality control was performed prior and after concatenation of the raw data with the tools *MultiQC* and *FastQC* respectively. All samples passed the quality check with most showing ~20% sequence duplication, sequence alignment greater or equal to 80%, below and below 50% GC coverage, all of which is acceptable and/or indicative of good quality for RNASeq samples [67,68]. Samples were then aligned, and counts were generated using the tools *HISAT2* (Galaxy Version 2.2.1+galaxy0, NCBI genome build GRCm38/mm10) and *featureCounts* (Galaxy Version 2.0.1+galaxy1), respectively. Differential expression analyses were performed with *limma* (Galaxy Version 3.48.0+galaxy1) [69] and Genome Set Enrichment Analysis (GSEA) with *fgsea* (Galaxy Version 1.8.0+galaxy1) [70] or GSEAPreranked (v6.0.12, https://gsea-msigdb.github.io/gseapreranked-gpmodule/v6/index.html) [64,71,72]. t-statistic metric for differential expression calculated with limma was used as the ranking metric for all GSEA analyses. GSEA plots were generated as previously described [73].

2.9 Immunoblot analysis

For immunoblotting analysis, cells growing in log phase in a 6 well dish were washed with 2mL of PBS and lysed in 100µL RIPA buffer [25 mM Tris-Cl, 150 mM NaCl, 0.5% sodium deoxycholate, 1% Triton X-100, 1x cOmplete protease inhibitor (Roche)]. Cells were scraped and the resulting lysate was clarified by centrifugation at 21,000xg for 10 min. Protein concentration of the lysate was determined by BCA assay (Thermofisher). Proteins (20–30µg) were resolved on SDS-PAGE, 4 to 12% Bis-Tris Gels (Invitrogen) and transferred to a polyvinylidene difluoride membrane using the iBlot 2 Dry Blotting System (Invitrogen). Membrane was blocked with Intercept Blocking Buffer (Li-cor) at room temperature for 2h, stained with primary and secondary antibodies and then visualized using a LI-COR imager with Image Studio software version 2.1.10.

The following primary antibodies were used: Ass1 (Atlas HPA020896; 1:200 dilution), Vinculin (Proteintech 66305-1-lg; 1:10000 dilution) and Beta-Actin (Proteintech 660009-1-lg; 1:10000 dilution). The following secondary antibodies were used: IRDye 680LT Goat Anti-Mouse Ig (Li-cor G926-68020; 1:10000 dilution) IRDye 800CW Goat anti-Rabbit IgG (Li-cor 926-32211; 1.:10000 dilution) and IRDye 800CW Goat anti-Mouse IgG (Li-cor 926-32210; 1:10000 dilution)

2.10 qRT-PCR analysis

RNA was extracted using the RNeasy Mini Kit and optional on-the-column DNAse digestion (Qiagen). Extracted RNA was converted to cDNA by reverse transcription using the High-Capacity cDNA Reverse Transcription Kit (Applied Biosystems). Expression levels of *Sdc1* transcript were amplified using PowerUp SYBR Green Master Mix (Invitrogen) and custom

primers. Quantification was performed using a QuantStudio 3 Real-Time PCR System (Applied Biosystems). The average change in threshold cycle (ΔCt) values was determined for each of the samples relative to *Gapdh* levels and compared with vehicle control (ΔΔCt). Finally relative gene expression was calculated as ($2^{-\Delta\Delta Ct}$). Experiments were performed in triplicate cultures.

2.11 GC-MS analysis of arginine

Dry polar metabolites extracts from intracellular extracts or media samples were derivatized with 16µL MOX reagent (ThermoFisher) for 1h at 37°C and then with 20µL 1% tert-butyldimethylchlorosilane in N-tert-Butyldimethylsilyl-N-methyltrifluoroacetamide (Sigma Aldrich) for 3h at 60°C. Derivatized samples were analyzed with an 8890 gas chromatograph system (Agilent Technologies) with a HP-5ms Ultra Inert column (Agilent Technologies) coupled with an 5997B Mass Selective Detector (MSD) mass spectrometer (Agilent Technologies). Helium was used as the carrier gas at a flow rate of 1.2 mL/min. One microliter of sample was injected in splitless mode at 280°C. After injection, the GC oven was held at 100°C for 1 min. and increased to 300°C at 3.5 °C/min. The oven was then ramped to 320°C at 20 °C/min. and held for 5 min. at this 320°C. The MS system operated under electron impact ionization at 70 eV and the MS source was held at 230 °C and quadrupole at 150 °C. The detector was set in scanning mode with a scanned ion range of 100–650 m/z. Metabolite were identified using fragments for each individual metabolite as previously described [74] and quantified by integration of peak area.

2.12 Isotopic labeling experiments in cell culture and intracellular metabolite extraction

To measure steady state labeling of polar metabolites by citrulline in cultured cells, triplicate cultures of 150,000 cells/well were seeded in a 6 well dish in 2 mL of medium. Cells were allowed to attach overnight. The following day cells were washed twice with PBS and then incubated with 8mL for 8 or 24h in TIFM with $^{13}C_5$-citrulline (Cambridge Isotope Laboratories, CLM-8653) added at TIFM concentrations. Immediately after the labeling period, cells were quickly washed with ~8mL of ice-cold blood bank saline. Cellular metabolites were extracted with addition of 600µL of an ice-cold methanol followed by scraping the cells on ice. The solution was then vortexed for 10 min, and centrifuged at 21,000xg for 10 min. 450µL of each extract was aliquoted to fresh sample tubes, dried under nitrogen gas and stored at -80°C before further analysis. Dried-down cell extracts were re-suspended with 75 µL of 60/40 acetonitrile/water, vortexed, incubated on ice for 20 minutes, and centrifuged for 30 minutes at 4°C and 20,000 g. The pooled QC samples were generated by combining ~20µL from each sample and injected regularly throughout the analytical batch.

2.13 CRISPR knockout and re-expression of *Ass1*

sgRNAs targeting *Ass1* were generated through the Broad Institute's Genetic Perturbation Platform Web Portal (https://portals.broadinstitute.org/gpp/public/). Oligonucleotide pairs were manufactured by Integrated DNA Technologies (IDT) and cloned into lentiCRISPRv2 (Addgene: #52961) as previously described [75,76]. HEK293T cells (Dharmacon) were transfected with the *Ass1* targeting lentiCRISPRv2 vectors and the lentiviral packing plasmids psPAX2 (Addgene:

#12260) and pMD2.G (Addgene: #12259). The medium was replaced after 24h, and lentivirus was harvested after 48h. Subconfluent mPDAC3-TIFM cells were infected with lentivirus using 8μg/mL polybrene and infected cells were selected in 2μg/mL puromycin and maintained with 100μM arginine. Single cell clones with immunoblot-confirmed loss of Ass1 were selected. A single cell clone without detectable Ass1 expression was transformed with a lentivirus produced as above with a vector encoding CMV-driven murine *Ass1* cDNA that would not be targeted by the *Ass1* sgRNA (VectorBuilder).

2.14 shRNA knockdown of *Sdc1*

Hairpin sequences targeting *Sdc1* were obtained from [77]. Oligonucleotide pairs were manufactured by IDT and cloned into a lentiviral LT3GEPIR vector (Addgene: #111177) to allow for doxycycline-inducible repression of gene expression. Lentiviral transfection and transformation were performed as described in **CRISPR knockout and re-expression of *Ass1*** and successfully transformed cells were selected and maintained with 2μg/mL puromycin. Cells transformed with LT3GEPIR with a *Renilla* luciferase targeting shRNA were used as a control.

2.15 Analysis macropinocytic capacity by DQ-BSA

The macropinocytic capacity of PDAC cells was assessed using a DQ Red BSA (Invitrogen) uptake assay. Cells were seeded at either 15,000 cells/well for 12 wells or 50,000 cells/well for 6 wells and allowed to attach over night. The following day the media was replaced with fresh media + 0.02mg/mL of the DQ Red BSA fluorogenic substrate and cells were harvested at different timepoints for up to 6 hours. Cells were then washed with PBS, trypsinized, washed

again with PBS, fixed in 4% paraformaldehyde for 15 minutes at 4ºC and DQ Red BSA fluorescence was quantified by flow cytometry in at least 10,000 cells per sample.

2.16 Animal experiments

Animal experiments were approved by the University of Chicago Institutional Animal Care and Use Committee (IACUC, Protocol #72587) and performed in strict accordance with the Guide for the Care and Use of Laboratory Animals of the National Institutes of Health (Bethesda, MD). Mice were housed in a pathogen-free animal facility at the University of Chicago with a 12 h light/12 h dark cycle, 30–70% humidity and 68–74°F temperatures maintained.

2.16.1 Orthotopic tumor implantation and monitoring

C57BL6J mice 8-12 weeks of age were purchased from Jackson Laboratories (Strain #:000664). 250,000 cells were resuspended in 20µL of 5.6mg/mL Cultrex Reduced Growth Factor Basement Membrane Extract (RGF BME; R&D Biosystems #3433-010-01) and serum-free RPMI solution. The BME:cellular mixture was injected into the splenic lobe of the pancreas of the mice as previously described [78] to generate orthotopic tumors. After implantation mice, were monitored daily by abdominal palpation.

2.16.2 In vivo Arg1 knockout

C57BL6J *Lyz2-Cre* and $Arg1^{fl/fl}$ mice were bred to generate *Lyz2-Cre* $^{+/+}$*;* $Arg1^{fl/fl}$ and litter mate control $Arg1^{fl/fl}$ mice. Animal husbandry was carried out in strict accordance with the

University of Chicago Animal Resource Center guidelines. Tumor implantation as described above was performed in mice at 8-12 weeks of age.

2.16.3 In vivo arginase-1 pharmacological inhibition

Orthotopic tumors were implanted in C57BL6J mice at 8-12 weeks of age. 4 weeks after induction, animals were treated with CB-1158. CB-1158 (MedChem Express) dissolved in sterile water was administered by oral gavage at 100mg/kg as previously described [79]. The acidity caused by the HCl in the drug solution was neutralized by adding an equivalent amount of NaOH. Control mice were treated with an equivalent amount of NaCl dissolved in sterile water as the vehicle. 2hrs after treatment with CB-1158 or vehicle, mice were euthanized by cervical dislocation, and tumors were harvested for TIF extraction.

2.16.4 In vivo $^{15}N_2$-glutamine tracing by bolus tail vein injections

Orthotopic tumors were implanted in C57BL6J mice at 8-12 weeks of age. 4 weeks after induction tumor-bearing mice and healthy littermate controls were treated with $^{15}N_2$-glutamine (Cambridge Isotope Laboratory #NLM-1328-PK) dissolved in sterile phosphate buffered saline at 7.2mg/animal by tail vein injection as previously described [80]. Briefly, animals were dosed three times at 15-minute intervals. 15 minutes after the final dose, ~100uL of blood were be obtained by submandibular sampling as described previously (Parasuraman et al., 2010) and animals were euthanized. The tumor or pancreas from each animal was then harvested and immediately snap frozen using a BioSqueezer (BioSpec) cooled with liquid nitrogen and stored at -80°F until further analysis.

2.16.5 In vivo $^{15}N_2$-glutamine tracing by jugular vein infusion

6~8-month-old female & male *Lyz2-Cre $^{+/+}$; Arg1$^{fl/fl}$* and litter mate control *Arg1$^{fl/fl}$* mice with mPDAC3-TIFM orthotopic tumors underwent dual jugular vein & carotid artery catheterization surgery. On day 5 of post recovery, mice received a 0.28 mg/g 10 min. bolus followed by a continuous 4 hr. infusion 0.005 mg/g/min infusion of $^{15}N_2$-glutamine (Cambridge Isotope Laboratory #NLM-1328-PK). Plasma samples were taken at time points: 0, 15, 30, 60, 120, 180, and 240 minute time points. Tumors and tissues were harvested at 240 min. and immediately snap frozen with liquid nitrogen stored at -80°C prior to analysis.

2.16.6 IF isolation from PDAC tumors

IF was isolated from tumors as described before [40]. Briefly, tumors were rapidly dissected after euthanizing animals. Tumors were weighed and rinsed in blood bank saline solution (150 mM NaCl) and blotted on filter paper (VWR, Radnor, PA, 28298–020). The process of dissection and tumor preparation took < 3min. Tumors were cut in half and put onto 20µm nylon mesh filters (Spectrum Labs, Waltham, MA, 148134) on top of 50 mL conical tubes, and centrifuged for 10min. at 4°C at 400xg. IF was then collected, snap-frozen in liquid nitrogen and stored at -80°C until further analysis.

2.17 Preparation of plasma and tumor samples from $^{15}N_2$-glutamine tracing experiments for LC-MS analysis

2.17.1 Metabolite extraction and sample analysis from bolus $^{15}N_2$-glutamine delivery tracing experiment

Cryogenically frozen tumor pieces were ground to a fine homogenous powder with a liquid nitrogen cooled mortar and pestle. ~30mg of tissue powder was weighed into sample tubes, and metabolites were extracted with 600µL HPLC grade methanol, 300µL HPLC grade water, and 400µL chloroform. Samples were vortexed for 10min at 4°C, centrifuged 21,000xg at 4°C for 10 min. 400µL of the aqueous top layer was removed into a new tube and dried under nitrogen. Dried tumor extracts were resuspended in 100µL HPLC grade water prior to analysis. Plasma samples (10µL) were extracted with 90 ul of 75:25:0.2 HPLC grade acetonitrile:methanol:formic acid extraction mix. Samples were vortexed for 5 min at 4°C and centrifuged at 4°C at maximum speed for 10 min. 80µl of supernatant were aliquoted to a fresh tube prior to analysis. LC-MS analysis for both tumor and plasma samples was performed as described before [40,59]. XCalibur 2.2 software (Thermo Fisher Scientific) was used identification and relative quantification for metabolites. Natural abundance correction was performed using the IsoCor [81].

2.17.2 Metabolite extraction from in vivo $^{15}N_2$-glutamine infusion tracing experiment

Plasma samples (10µL) were extracted with 40 µL of ice-cold methanol, vortexed for 5 minutes at 4°C using an Eppendorf ThermoMixer, incubated on ice for 20 minutes, and centrifuged

for 30 minutes at 4°C at 20,000 g. The supernatant was dried down using a Genevac EZ-2.4 elite evaporator. Dried-down samples were re-suspended in 60 µL of 60/40 acetonitrile/water before LC-MS analysis. The snap-frozen tissue and tumor samples were ground to a powder using a mortar and pestle on dry ice, extracted with ice-cold 4/4/2 acetonitrile/methanol/water (20 µL solvent/mg of tissue), vortexed for 5 minutes at 4°C using an Eppendorf ThermoMixer. Samples were incubated on ice for 20 minutes, centrifuged for 30 minutes at 4°C at 20,000 g and 600 µL of supernatant was dried down and stored at -80°C. Samples were re-suspended in 100 µL of 60/40 acetonitrile/water prior to LC-MS analysis described below.

2.17.3 LC-MS data acquisition and analysis for in vivo $^{15}N_2$-glutamine infusion tracing and in vitro $^{13}C_5$-citrulline experiments

Metabolite separation was performed using Thermo Scientific Vanquish Horizon UHPLC system and Atlantis BEH Z-HILIC (2.1x150 mm, 2.5 µM; part # 186009990; Waters Corporation) column at acidic pH or a iHILIC-(P) Classic (2.1x150 mm, 5 µm; part # 160.152.0520; HILICON AB) column at basic pH. For the acidic pH method, the mobile phase A (MPA) was 10 mM ammonium formate containing 0.2% formic acid and mobile phase B (MPB) was acetonitrile containing 0.1% formic acid. The column temperature, injection volume, and flow rate were 30°C, 5 µL, and 0.2 mL/minute, respectively. The chromatographic gradient was 0 minute: 90% B, 15 minutes: 20% B, 16 minutes: 20% B, 16.5 minutes: 90% B, 17 minutes: 90% B, and 23 minutes: 90% B. The flow rate was increased to 0.4mL/minute for 4.7 minutes during the re-equilibration. MS detection was done using Orbitrap IQ-X Tribrid mass spectrometer (Thermo Scientific) with a H-ESI probe operating in switch polarity mode for both methods except the *in vitro* $^{13}C_5$ citrulline tracing

experiment data were data was collected only in positive mode. MS parameters were as follows: spray voltage: 3800 V for positive ionization and 2500 V for negative ionization modes, sheath gas: 80, auxiliary gas: 25, sweep gas: 1, ion transfer tube temperature: 300°C, vaporizer temperature: 300°C, automatic gain control (AGC) target: 25%, and a maximum injection time of 80 milliseconds (ms).

For the basic pH method, MPA was 20 mM ammonium bicarbonate at pH 9.6, adjusted by ammonium hydroxide addition and MPB was acetonitrile. The column temperature, injection volume, and the flow rate were 40°C, 2 µL, and 0.2mL/minute, respectively. The chromatographic gradient was 0 minute: 85% B, 0.5 minute: 85% B, 18 minutes: 20% B, 20 minutes: 20% B, 20.5 minutes: 85% B and 28 minutes: 85% B. MS parameters were as follows: spray voltage:3600V for positive ionization and 2800 for negative ionization modes, sheath gas: 35, auxiliary gas: 5, sweep gas: 1, ion transfer tube temperature: 250°C, vaporizer temperature: 350°C, AGC target: 100%, and a maximum injection time of 118 ms.

For both methods, data acquisition was done using the Xcalibur software (Thermo Scientific) in full-scan mode with a range of 70-1000 m/z at 120K resolution (acidic pH) and 60K (basic pH). Metabolite identification was done by matching the retention time and MS/MS fragmentation to the reference standards. Data analysis was performed using Tracefinder 5.1 software (Thermo Scientific).

2.18 HPLC-MS-MS analysis amino acid levels in PDAC IF samples upon arginase inhibition

IF samples were analyzed by High-Performance Liquid Chromatography and Tandem Mass Spectrometry (HPLC-MS-MS) using a Thermo Q-Exactive in line with an electrospray source and an Ultimate3000 (Thermo) series HPLC consisting of a binary pump, degasser, and auto-sampler outfitted with a Xbridge Amide column (Waters; dimensions of 3.0 mm × 100 mm and a 3.5 µm particle size). The mobile phase A contained 95% (vol/vol) water, 5% (vol/vol) acetonitrile, 10 mM ammonium hydroxide, 10 mM ammonium acetate, pH = 9.0; B was 100% Acetonitrile. The gradient was as following: 0 min, 15% A; 2.5 min, 64% A; 12.4 min, 40% A; 12.5 min, 30% A; 12.5-14 min, 30% A; 14-21 min, 15% A with a flow rate of 150 µL/min. The capillary of the ESI source was set to 275 °C, with sheath gas at 35 arbitrary units, auxiliary gas at 5 arbitrary units and the spray voltage at 4.0 kV. In positive/negative polarity switching mode, an m/z scan range from 60 to 900 was chosen and MS1 data was collected at a resolution of 70,000. The automatic gain control (AGC) target was set at 1 × 106 and the maximum injection time was 200 ms. The targeted ions were subsequently fragmented, using the higher energy collisional dissociation (HCD) cell set to 30% normalized collision energy in MS2 at a resolution power of 17,500. Besides matching m/z, target metabolites are identified by matching either retention time with analytical standards and/or MS2 fragmentation pattern. Data acquisition and analysis were carried out by Xcalibur 4.1 software and Tracefinder 4.1 software, respectively (both from Thermo Fisher Scientific).

2.19 Measuring intratumoral and IF concentrations of amino acids

To quantitatively measure IF amino acid abundance, polar metabolites were extracted from 5μL IF samples using 45μL 75:25:0.1 HPLC grade acetonitrile:methanol:formic acid extraction mix into which a mixture of isotopically labeled amino acids of known concentrations (Cambridge Isotope Laboratories, MSK-A2-1.2) was added. Samples were vortexed for 10 min, and centrifuged at maximum speed for 10 min. 30 μL of each extract was removed and dried under nitrogen gas and stored −80°C until further analysis. LC-MS analysis and calculating amino acid concentration in these samples was performed as in **Quantification of metabolite levels in cell culture media**.

To measure amino acid amounts in tumor samples, intratumoral metabolites were extracted from ~30mg of tumor tissue and dried down as described in **Preparation of plasma and tumor samples from $^{15}N_2$-glutamine tracing experiments for LC-MS analysis**. Dried samples were rehydrated with 2:1 methanol:water into which a mixture of isotopically labeled amino acids of known concentrations (Cambridge Isotope Laboratories, MSK-A2-1.2) was added. Samples were then analyzed by LC-MS as described in **Quantification of metabolite levels in cell culture media**. Amino acid amounts in a given mass of tumor were determined by comparison of peak areas of unlabeled amino acids with peak areas of labeled amino acids that were present at known amounts and dividing by the mass of tumor extracted.

To compare metabolite concentrations between tumor and TIF samples, the density for orthotopic mPDAC tumors was needed to convert amino acid amount per unit tumor mass into a concentration (amino acid amount per unit volume). The density of freshly isolated mPDAC3-RPMI tumors was determined by measuring tumor mass and calculating the volume (V) of the tumors with the following formula:

$V = 4/3 * \pi * A * B * C$

where A, B, C are the lengths of the semi-axes of an ellipsoidal shape, which were measured from tumors with an electronic caliper (Thermofisher). Tumor density was then calculated by dividing the tumor mass by the calculated volume. Tumor density was then used to convert amino acid amount per tumor mass measurements into an intratumoral concentration.

2.20 Human samples regulation

Human histology samples were obtained under approval by the Institutional Review Boards at the University of Chicago (IRB 17-0437).

2.21 Immunohistochemistry

For ARG1 and ASS1 staining, the slides were stained using Leica Bond RX automatic stainer. Dewax (AR9222, Leica Microsystems) and rehydration procedure were performed in the system and a 20 min treatment of epitope retrieval solution I (Leica Biosystems, AR9961) was applied. anti-Arginase-1 (1:100, Cell Signaling #93668) or anti-Ass1 (1:100, Atlas HPA020896;) and were applied on tissue sections for 60min. Antigen-antibody binding was detected using Bond polymer refine detection (Leica Biosystems, DS9800). The tissue sections were counter stained with hematoxylin and covered with cover glasses.

For F4/80 staining, tissue sections were deparaffinized and rehydrated with xylenes and serial dilutions of EtOH to deionized water. They were incubated in antigen retrieval buffer (DAKO, S1699) and heated in steamer at 97°C for 20 minutes. Anti-mouse F4/80 antibody (1:200, MCA497GA, AbD Serotec) was applied on tissue sections for 1hr at room temperature. Tissue

sections were washed with Tris buffered saline and then incubated with biotinylated anti-rat IgG (10 μg/ml, BA-4001, Vector laboratories) for 30 min at room temperature. Antigen-antibody binding was detected by Elite kit (PK-6100, Vector Laboratories) and DAB (DAKO, K3468) system.

Slides were scanned using the Aperio ScanScope slide scanner and images were stored and analyzed with Aperio eSlideManager and Aperio ImageScope (version 12.4.6.5003) respectively Algorithm (Leica Biosystems Imaging, Inc.). Annotation and quantification of slides were supervised by a trained pathologist (Chris Weber) in a blinded fashion and regions for each experiment were annotated as described in figure legends. Staining coverage and intensity in the annotated regions were quantified using the Aperio Positive Pixel Count Algorithm (Leica Biosystems Imaging, Inc.), unmodified. Briefly, to calculate staining coverage for each annotated region, the total amount of stain positive pixels (as defined by the algorithm) was counted and classified for Low, Medium or High Intensity. Each intensity group was assigned a relative numeric value (Low = 1, Medium = 2, High = 3). The stain intensity value was then multiplied by the total number of positive pixels in each group, for each annotated region. The resulting values were then normalized to the total number of pixels in the analyzed region. These normalized staining intensity values were then averages for all analyzed regions in each histological sample.

CHAPTER 3

PDAC CELLS GROWN IN TUMOR INTERSTITIAL FLUID-BASED CULTURE MEDIUM RECAPITULATE THE TRANSCRIPTOMIC BEHAVIOR OF PDAC CELLS GROWING *IN VIVO*

3.1 Introduction

Tumor metabolism differs markedly from that of untransformed tissues[82], which is driven in part by the influence of cell-intrinsic factors, such as oncogenic lesions[9]. However, cell-extrinsic factors in the tumor microenvironment (TME) also play a substantial role in regulating tumor metabolism[11,12,21]. Indeed, tumors have a substantially different microenvironment compared to normal tissues, and these microenvironmental abnormalities also contribute to the metabolic abnormalities observed in tumors. Thus, to better understand the contribution of metabolism to tumor biology, I am seeking to understand how cell extrinsic cues in the TME shape intracellular metabolic pathways.

One such cell-extrinsic microenvironmental factor that strongly influences cancer cell metabolism is nutrient availability[83–85]. Factors such as vascularization, stromal composition, and immune cell infiltration influence nutrient delivery to tissues and these factors are abnormal in tumors, leading to altered nutrient availability in the TME[11,86,87], which could impact cancer cell metabolism. Despite the potential role of extracellular nutrient availability in shaping tumor metabolism, our knowledge of how this cell extrinsic cue impacts tumor metabolism is limited as we have had little understanding of TME nutrient levels.

To overcome this limitation, we developed a workflow to isolate interstitial fluid (IF), the perfusate of solid tissues and tumors, in murine models of pancreatic adenocarcinoma (PDAC) and profile the concentrations of metabolites[40]. In contrast to healthy tissues where nutrient levels in the interstitial fluid are comparable to plasma nutrient levels[88], we found that PDAC IF had substantially altered nutrient levels compared to the plasma, as has also been shown in other cancers including renal cell carcinoma and glioblastoma[52,89]. Thus, we now have a more complete understanding of TME nutrient availability in PDAC and are poised to use this to understand how this cell extrinsic factor impacts cancer cell metabolism.

3.2 Results

To study how the nutrient composition of the PDAC TME influences cancer cell biology, we developed a cell culture medium termed Tumor Interstitial Fluid Medium (TIFM) based on metabolite concentrations in PDAC IF [40]. To do so, we used an approach similar to those described for the generation of media with plasma levels of nutrients [90,91] (Fig. 3.1A). TIFM is composed of 115 metabolites at the average concentration previously observed in the IF of *Kras*$^{LSL\text{-}G12D/+}$; *Trp53*$^{fl/fl}$; *Pdx1*^{Cre} [40,92] murine PDAC tumors. These metabolites were selected on the following bases: (1) commercial availability at high purity, (2) stability in aqueous solution, and (3) presence in PDAC IF at a concentration > 0.5μM. To enable rapid identification of bio-active nutrients, TIFM is composed of 9 pools of metabolites that are separately compounded [90,91].

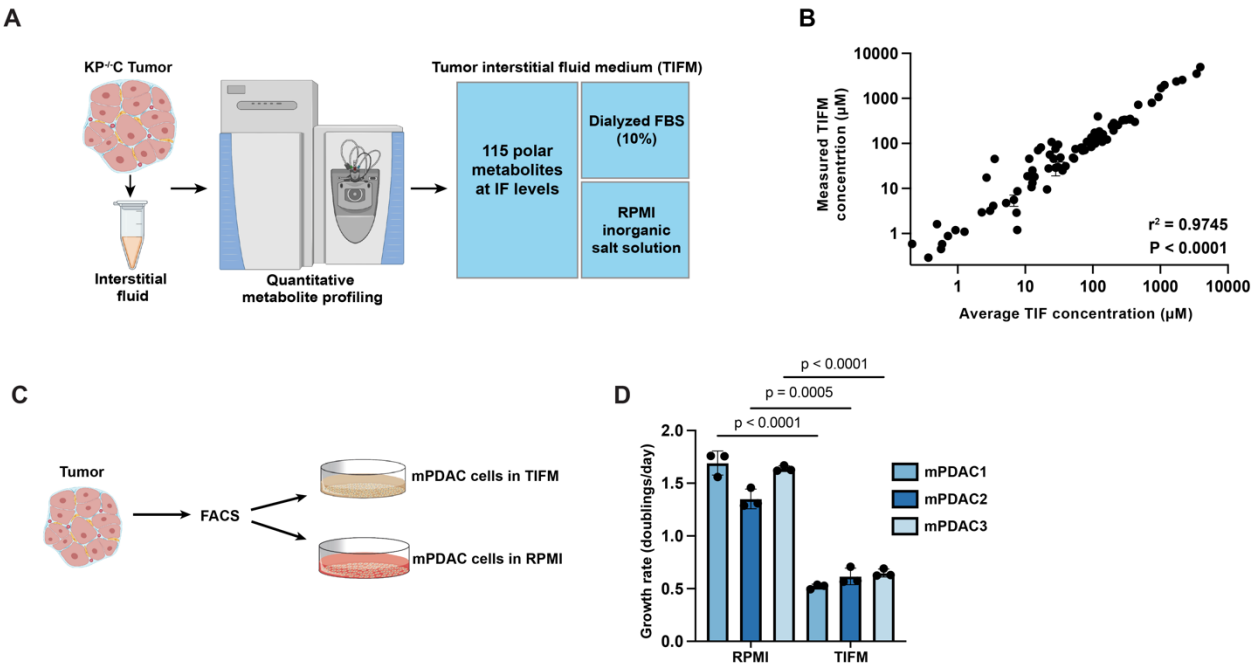

Figure 3.1. Tumor Insterstitial Fluid Medium sustains murine PDAC cell growth. (A) Diagram of the Tumor Interstitial Fluid Medium (TIFM) formulation. (B) Scatter plot of LC-MS measurements of metabolite concentrations in TIFM (n=6) plotted against expected concentrations of the metabolite in TIFM (average concentration of the given metabolite in mouse PDAC TIF). The values represent the mean of LC-MS measurements, and the error bars represent ± SD. r^2 and p-value were determined by Pearson correlation. (C) Diagram of the generation of paired PDAC cell lines grown in TIFM or in RPMI isolated from mouse PDAC tumors. PDAC tumors were used for the IF measurements on which the TIFM formulation is based. (D) Cell proliferation rate of paired mPDAC cell lines grown in TIFM or RPMI (n=3). The values represent the mean and the error bars represent ± SD. Statistical significance was calculated using a two-tailed Student's t test.

To generate the complete medium, the individual metabolite powders are reconstituted in water along with salts at RPMI-1640 (RPMI) concentrations and 10% dialyzed fetal bovine serum (dFBS) to provide lipids, growth factors, and any other macromolecules necessary for cell growth. Sodium bicarbonate is also added at RPMI concentrations to maintain physiological pH [93]. Importantly, quantitative metabolite profiling by liquid chromatography-mass spectrometry (LC-MS) of TIFM confirmed that TIFM contained metabolites at expected concentrations (Fig. 3.1B). Thus, TIFM recapitulates the nutrient microenvironment of PDAC.

To determine if TIFM could sustain cancer cells, we isolated murine PDAC (mPDAC) cell lines from three individual mouse PDAC tumors by fluorescence activated cell sorting (FACS). This PDAC model is the same mouse model used for TIF metabolomics analyses and which formed the basis of TIFM composition [40]. We then split the cells isolated from each tumor into two populations, which were cultured either in TIFM or standard culture conditions (RPMI-1640) to generate paired mPDAC cell lines termed mPDAC-RPMI or mPDAC-TIFM (Fig. 3.1C). mPDAC-TIFM cells readily proliferate in TIFM culture, albeit at a slower rate than in RPMI-1640 (Fig. 3.1D), suggesting that TIFM has the necessary nutrients to sustain PDAC cell proliferation. Interestingly, while mPDAC-TIFM cells continue proliferating when transitioned directly from culture in TIFM to RPMI-1640, transferring mPDAC-RPMI cells directly to TIFM results in near-complete arrest of cell growth (Fig. 3.2). This suggests that long term growth of mPDAC cells in standard cell culture media results in loss of key adaptations to grow under TME nutrient stress. Thus, analysis of PDAC cell metabolism in TIFM could identify novel metabolic adaptations required for growth under TME conditions that would not be apparent from studying PDAC cells under standard culture conditions.

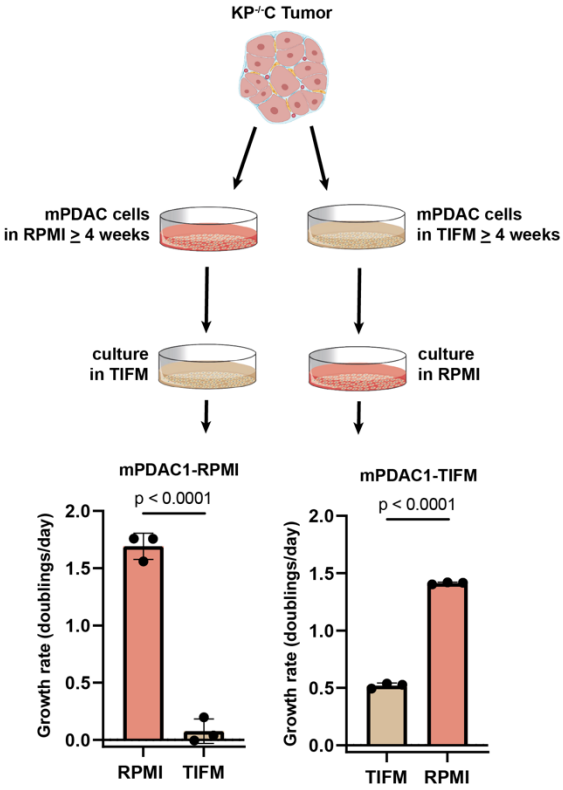

Figure 3.2. mPDAC cells cannot proliferate in TIFM after long term culture in RPMI. mPDAC cells were isolated from a mouse PDAC tumor and cultured directly in TIFM or RPMI. After long term culture (>1 month) in either media condition, cells were plated into the other media (i.e. cells grown in TIFM were subsequently cultured in RPMI and cells grown to RPMI were subsequently grown in TIFM, as indicated). The proliferation rate of the cells upon switching media conditions was measured (n=3). The values represent the mean and the error bars represent ± SD and statistical significance was calculated using a two-tailed Student's t test. (n=3). The values represent the mean and the error bars represent ± SD. Statistical significance was calculated using a two-tailed Student's t test.

To identify such adaptations, we performed transcriptomic profiling comparing gene expression patterns of the same mPDAC cells (mPDAC3-TIFM) isolated by FACS: (1) after culture in TIFM, (2) after culture in RPMI-1640 and (3) after growing as syngeneic orthotopic murine tumors to provide an *in vivo* reference (Fig. 3.3A). This experimental design allowed us to identify transcriptionally-driven metabolic adaptations in TIFM and confirm these were operative *in vivo*. Further, the *in vivo* transcriptomic data allows us to assess how the transcriptional state of PDAC cells in different *ex vivo* models compares to the *bona fide in vivo* cell state. This analysis has recently been suggested to be a critical benchmark for assessing *ex vivo* model fidelity [94]. We first established that compared to standard culture conditions, mPDAC cells in orthotopic tumors substantially alter their transcriptional profile (Fig. 3.3B). The majority of detected transcripts (12,066/16,378) are differentially expressed in the same mPDAC cells when grown *in vivo* compared to standard culture conditions.

Next, using this differential expression data, we generated gene sets of the most significantly upregulated and downregulated genes in mPDAC cells growing *in vivo* compared to RPMI ('top 500 genes up in vivo' and 'top 500 genes down in vivo' respectively). We then performed gene set enrichment analysis (GSEA) [72,95] using the transcriptomic data of mPDAC3-TIFM cells growing in TIFM and RPMI using the 'top 500 genes up in vivo' and 'top 500 genes down in vivo' gene sets. Compared to mPDAC cells cultured in RPMI, mPDAC cells in TIFM show a strong enrichment for *in vivo* upregulated genes and negative enrichment for genes downregulated *in vivo* (Fig. 3.3C). While limiting these gene sets to 500 genes ensures there is no enrichment score inflation due to the large gene set size [72], using gene sets comprised of all 5000+ genes significantly up or downregulated for each set generates the same enrichment patterns

Figure 3.3. (following page) Genome set enrichment analysis (GSEA) shows mPDAC cells cultured in TIFM better recapitulate the transcriptomic behavior of PDAC cells *in vivo*. (A) Diagram of workflow for the transcriptomic comparison of mPDAC3-TIFM cells grown in TIFM (n=3), RPMI (n=3) or as orthotopic allograft murine tumors (n=6). mPDAC cells from each condition were isolated by FACS and RNA was isolated for transcriptomic analysis by next generation sequencing. (B) Volcano plot of differentially expressed genes (DEGs) between mPDAC3-TIFM cells growing *in vivo* vs. cultured in RPMI (Tumor/RPMI). Blue: downregulated genes in tumors with adjusted $p<0.05$. Red: upregulated genes in vivo with adjusted $p<0.05$. Gray: genes with adjusted $p>0.05$. Adjusted p-value was calculated using Limma with the Benjamini and Hochberg false discovery rate method (Benjamini & Hochberg, 1995) (C) GSEA of transcriptomic data from mPDAC3 cells cultured in TIFM versus mPDAC3 cells cultured in RPMI using custom gene sets generated from DEG analysis in (B), each with top 500 upregulated (top) or downregulated (bottom) genes as determined by adjusted p-value. Genes are ranked by t-statistic metric for differential expression between TIFM and RPMI cultured mPDAC3-TIFM cells calculated with limma. The top segment of each signature plot shows the running enrichment score for the gene set as the analysis progresses down the ranked list. The bottom segment of each signature plot shows where each member of the gene set as it appears in the ranked gene list. (D) Same analysis as in (C) with custom gene sets using all differentially upregulated (top) or downregulated (bottom) genes from DEG analysis in (B), as determined by adjusted $p<0.05$.

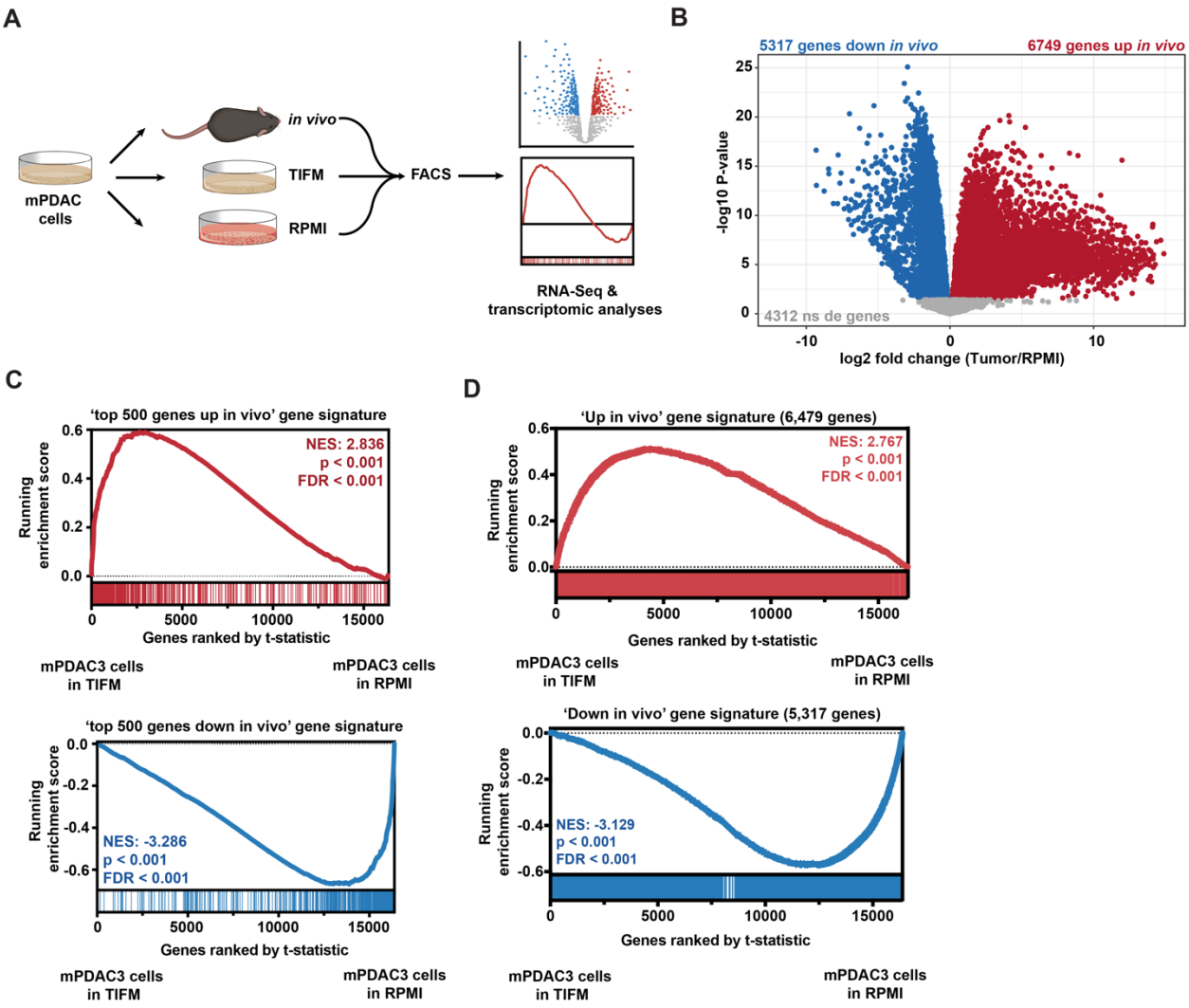

with similar enrichment scores (Fig. 3.3D). We also found a strong correlation between gene expression changes induced by culture in TIFM and growth *in vivo* (Fig. 3.4A). Lastly, among the top 20 up- and downregulated curated gene signatures from MSigDB [72,95] in TIFM cultured mPDAC cells compared to RPMI, most were similarly up or down-regulated *in vivo* compared to RPMI (Fig. 3.4B). Altogether, this analysis demonstrates that gene expression in TIFM cultured mPDAC cells more closely aligns with the gene expression pattern of mPDAC cells *in vivo*.

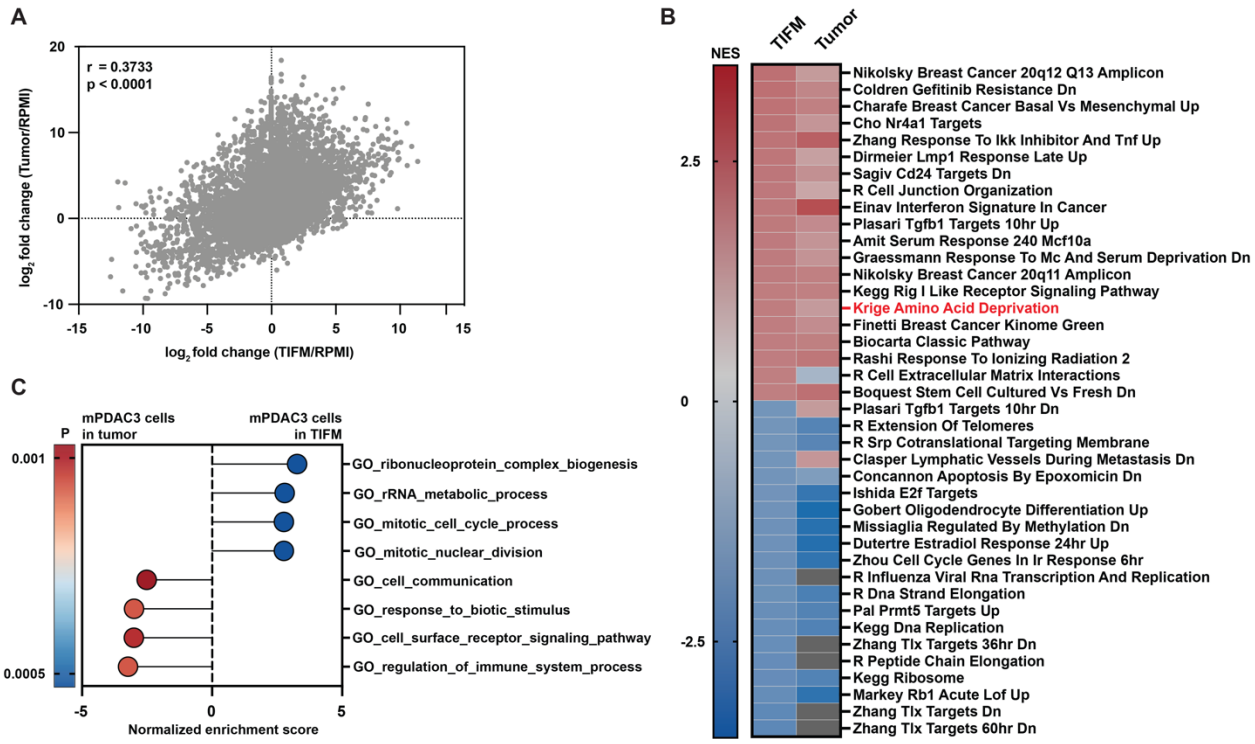

Figure 3.4. TIFM is a useful model for the discovery of cancer cell adaptations to physiological tumor nutrient stress in PDAC. (A) Log_2 fold changes in mean gene expression between mPDAC3-TIFM cells in TIFM (n=3) versus RPMI (n=3) (x axis) compared to mPDAC3-TIFM cells *in vivo* (n=6) versus in RPMI (n=3) (y axis). Statistical significance was determined by Pearson correlation r = 0.3733, p<0.0001. (B) (*left column*) Heatmap of normalized enrichment scores (NES) for top 40 enriched or depleted gene sets from MsigDB curated gene set (C2) collection in mPDAC3-TIFM cells cultured in TIFM vs. mPDAC3 cells cultured in RPMI. (*right column*) NES for these gene sets in mPDAC3-TIFM cells grown *in vivo* versus in RPMI. Grey boxes represent gene sets not differentially enriched between conditions. (J) Main cellular processes differentially expressed in mPDAC3-TIFM cells grown TIFM versus *in vivo* (TIFM/*in vivo*) as determined by GSEA analysis with MsigDB GO-based (C5) gene set collection. Only gene sets with an nMoreExtreme = 0 were considered in this analysis. For GO gene sets with overlapping genes and enrichment scores driven by the same set of differentially expressed genes, the largest gene sets containing these differentially expressed genes were selected for display.

We also sought to understand which aspects of the *in vivo* mPDAC cell state were not recapitulated in TIFM. To identify the cellular processes that are differentially regulated between cells growing in TIFM and cells *in vivo*, we performed GSEA using Gene ontology (GO) based gene sets on transcriptomic data from mPDAC3-TIFM cells *in vivo* and in TIFM. The main cellular processes differentiating PDAC cells growing *in vivo* from cells growing in TIFM are cell-cell

communication, response to biotic stimuli, cell surface receptor activated pathways, and regulation of the immune system (Fig. 3.4C). These differences are likely due to the presence of the immune compartment and other neighboring cell populations in PDAC tumors, an aspect of the TME not modeled in TIFM. On the other hand, the main cellular processes positively enriched in PDAC cells in TIFM relative to *in vivo* are ribosome complex biogenesis, rRNA processing, and mitotic cell division (Fig. 3.4C), suggesting that, although the slower proliferation of mPDAC cells in TIFM (Fig. 3.1D) is more reminiscent of cells *in vivo*, cell cycle progression and translation are nevertheless still higher in TIFM than *in vivo*. Altogether, these results show that mPDAC cells grown in TIFM more closely recapitulate the transcriptomic profile of cells growing directly in the TME, suggesting that TIFM is a useful system for the discovery and characterization of cancer cell adaptations to physiological tumor nutrient stress in PDAC.

3.3 Discussion

We directly assessed the impact of the TME on the cellular state of murine PDAC cells by transcriptomic analysis. We found that the TME does indeed induce substantial changes in the transcriptional state of PDAC cells compared to PDAC cells in standard culture, consistent with the microenvironment being an important regulator of cancer cell biology (Fig. 3.3B).

Given that metabolism is highly interconnected with epigenetic regulation of gene expression [96–99] and that cellular metabolism is intricately tied to nutrient availability [13,21], we reasoned that physiological nutrient availability could have dramatic influences on cellular state and be a key microenvironmental factor influencing cancer cell biology. Indeed, we found that growth of PDAC cells in physiological nutrition caused substantial transcriptional reprogramming, pushing PDAC cells towards a more *in vivo*-like transcriptional state compared to non-physiological

standard culture conditions (Fig. 3.3C, D & Fig. 3.4 A, B). Thus, consistent with recent studies that have incorporated physiological nutrient levels into cell culture systems [33,65,90,91], we have found that modeling physiological nutrient availability substantially improves cell culture model fidelity.

Thus, along with other efforts to improve the fidelity of cell culture models by incorporating microenvironmental factors such as bio-scaffolds enabling three-dimensional growth [100,101], we anticipate ensuring proper nutrient availability will be critical in the development of more physiologically relevant *ex vivo* cancer models, which will expand our ability to target cancer by enabling exploitation of microenvironmentally driven therapeutic targets [102,103].

CHAPTER 4

ARGININE BIOSYNTHESIS SUPPORTS PDAC CELL GROWTH UNDER TME NUTRIENT STRESS.

4.1 Introduction

Argininosuccinate synthase 1 (ASS1) is the rate-limiting enzyme in the biosynthetic pathway of the non-essential amino acid arginine [104]. ASS1 catalyzes the synthesis of argininosuccinate from citrulline and aspartate, which can then be converted to arginine and fumarate by argininosuccinate lyase (ASL). Thus, expression of ASS1 enables cells to synthesize arginine *de novo*. Arginine biosynthesis is a metabolically costly process due to its utilization of intracellular aspartate, a limiting nutrient for tumors [105,106]. Aspartate limitation that arises from arginine synthesis slows nucleotide production and, ultimately tumor growth [107]. Thus, ASS1 acts as a metabolic tumor suppressor and is silenced in many tumor types [108], making consumption of extracellular arginine essential in these cancers[109].

Arginine is one of the most limiting nutrients in the murine PDAC TME at 2-5μM relative to 125μM in plasma, a 20-50 fold decrease [40], leaving the TME level of arginine below the reported Km for arginine transport [110]. Arginine is a critical metabolite required for many cellular processes. It is a proteinogenic amino acid as well as the precursor for other metabolites necessary for cellular function [109]. Indeed, cells that become depleted of arginine undergo cell death [111,112]. As this metabolite is so central for cellular function, cells have evolved arginine sensors, which initiate cell growth only when arginine is available [113], and arginine metabolism is tightly regulated by a handful of enzymes, including ASS1 [114]. Transcriptomic analyses of PDAC cells growing under tumor microenvironmental nutrient levels, showed that these cells upregulate ASS1

in response to tumor nutrient stress, both in our TIFM system and *in vivo*. We hypothesized that mPDAC cells are starved of arginine in the TME, and expression of ASS1 provides mPDAC cells an alternative cellular arginine source.

4.2 Results

We sought to identify metabolic adaptations cancer cells exhibit in response to tumor nutrient stress using the transcriptional profiles of mPDAC cells in TIFM and *in vivo*. We focused on adaptation to amino acid deprivation, as this gene signature is highly enriched in TIFM (Fig. 4.1A) and is similarly enriched in mPDAC cells *in vivo* (Fig. 3.4B). Leading edge analysis [72] identified *Ass1* as the most differentially expressed gene in this signature (Fig. 4.1B). We further confirmed the upregulation of ASS1 at the protein level by immunoblotting for ASS1 in protein extracts from TIFM and RPMI cultured mPDAC cells (Fig. 4.1C). Immunohistological analysis of murine and

Figure 4.1. (following page) Upregulation of ASS1 is an adaptation of PDAC cells to tumor nutrient stress. (A) GSEA analysis of the MsigDB Krige_Amino_Acid_Deprivation signature in mPDAC3-TIFM cells cultured in TIFM versus in RPMI. (B) (*left*) Row-scaled heatmap of the $\log_2$ fold change of trimmed mean of M values (TMM) normalized gene counts for Krige_Amino_Acid_Deprivation genes in mPDAC3-TIFM cells cultured in TIFM versus RPMI. (*right*) t-statistic metric for differential expression calculated with limma for expression of indicated genes between mPDAC3-TIFM cells cultured in TIFM versus RPMI. (C) Immunoblot analysis of ASS1 in mPDAC cell lines grown in TIFM or RPMI as indicated. (D) (*left*) Representative images of immunohistochemical staining for ASS1 in $Kras^{LSL\text{-}G12D}$; $Trp53^{fl/fl}$; $Ptf1a^{CreER}$ murine PDAC tumors (n=6) and untransformed murine pancreas (n=8) as well as in human PDAC tumors (n=9) and untransformed human pancreas (n=6). Scale bar: 100μm. (*right*) IHC Scores were calculated as described in Chapter 2. Regions of ductal epithelial cells (for untransformed pancreas) and malignant (for PDAC tumors) cells were annotated for this analysis. Statistical significance was calculated using a two-tailed Student's t test.

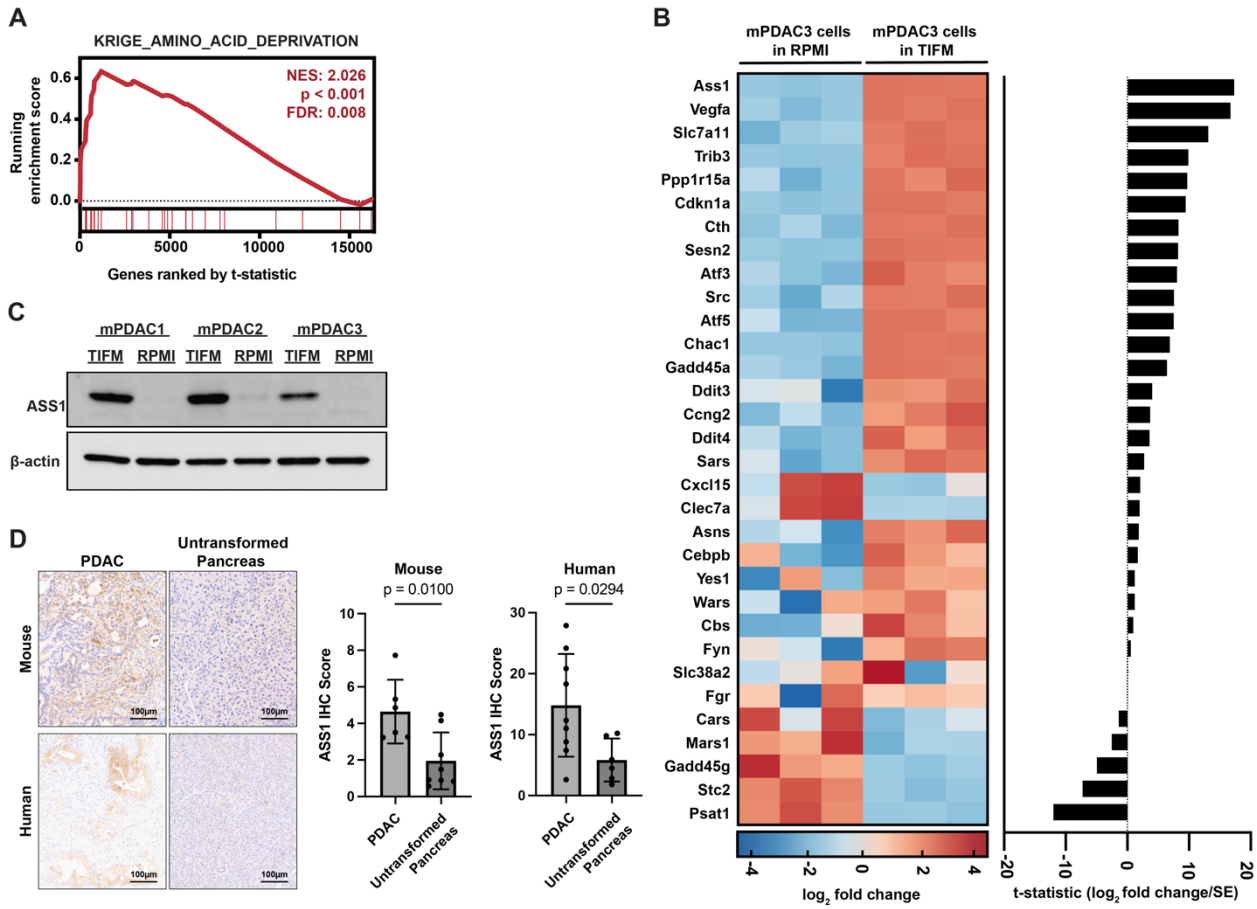

human PDAC tumors (Fig. 4.1D) shows similarly robust expression of ASS1, especially compared to the lack of expression in the untransformed exocrine pancreas. These data suggest that mPDAC cells express ASS1 in the TME or when exposed to TME nutrient stress.

ASS1 is the rate-limiting enzyme for the *de novo* biosynthesis of non-essential amino acid arginine. To test if mPDAC cells require *de novo* synthesis to maintain intracellular arginine pools, we first asked if mPDAC cells in TIFM consume the metabolic substrates (citrulline or ornithine) used for *de novo* arginine synthesis. To do so, we used quantitative LC-MS metabolite profiling [40] to perform an analysis of 108 metabolites that mPDAC1-TIFM and mPDAC1-RPMI cells consume or release in their respective media [63,64]. Interestingly, we found that mPDAC1-TIFM cells selectively consume citrulline, but not ornithine, at a rate similar to that of arginine uptake (Fig. 4.2A). Citrulline uptake by mPDAC cells in TIFM is consistent with active arginine synthesis

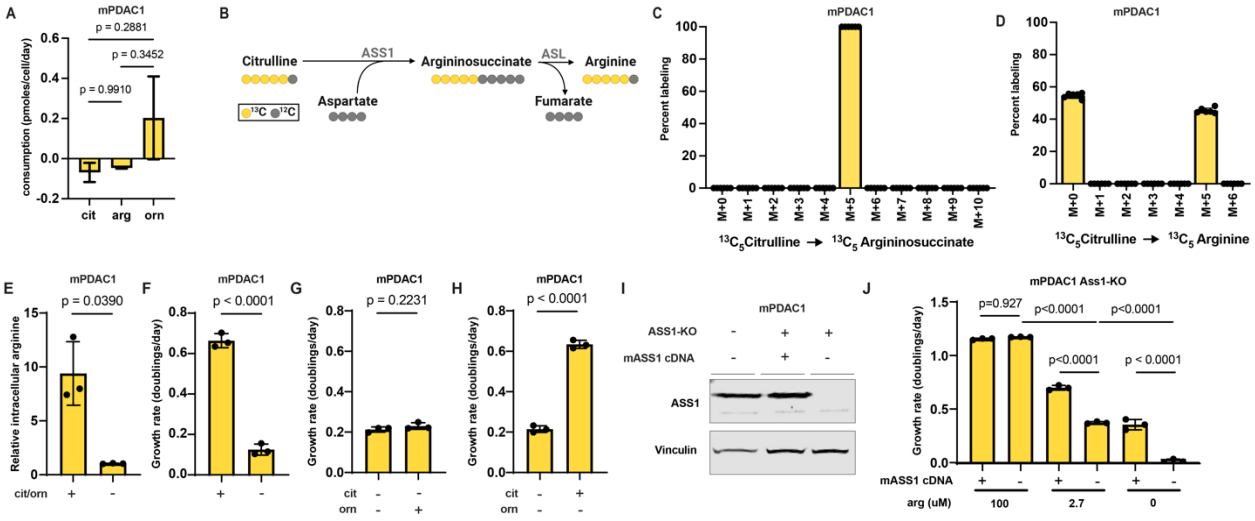

Figure 4.2. Arginine biosynthesis allows PDAC cells to adapt to low microenvironmental levels of arginine. (A) Cellular consumption/release rate of citrulline, ornithine and arginine by mPDAC1-TIFM cells cultured in TIFM (n=6). Statistical significance was calculated using an ordinary one-way ANOVA test with Tukey's multiple comparison correction. (B) Diagram showing the metabolic pathway mediating isotopic label incorporation from $^{13}C_5$-citrulline into arginine. (C) Mass isotopomer distribution of intracellular argininosuccinate and (D) intracellular arginine in mPDAC1 cells grown in TIFM with $^{13}C_5$-citrulline at PDAC IF concentration (67μM) (n=6). (E) Relative intracellular arginine levels of mPDAC1 cells grown in TIFM with (+) or without (-) TIF concentrations of citrulline (cit) and ornithine (orn). Statistical significance was calculated using a two-tailed Student's t test. (F) Proliferation rate of mPDAC1 cells in same conditions as (E) (n=3). Statistical significance was calculated using a two-tailed Student's t test. (F) Cell proliferation rate of mPDAC1-TIFM cells with or without TIFM concentrations of ornithine (orn) (n=3). Statistical significance was calculated using a two-tailed Student's t test. (G) Cell proliferation rate of mPDAC1-TIFM cells with or without TIFM concentrations of citrulline (cit) (n=3). Statistical significance was calculated using a two-tailed Student's t test. (H) mPDAC1-TIFM cells were infected with lentiviruses encoding a *Ass1* targeting CRISPR vector. *Ass1* knockout cells were then infected with lentiviruses expressing either CRISPR resistant *Ass1* cDNA or empty vector (E.V.), as indicated. An immunoblot analysis of ASS1 and vinculin (loading control) of protein lysates from these modified cells is shown. (I) Cell proliferation rate of cells in (J) grown in TIFM with different arginine concentrations as indicated (n=3). Statistical significance was calculated using an ordinary one-way ANOVA test with Tukey's multiple comparison correction.

in TIFM cultured mPDAC cells contributing substantially to intracellular arginine levels. To determine if citrulline consumption by PDAC cells enables arginine synthesis, we cultured mPDAC cells in TIFM with isotopically labeled $^{13}C_5$-citrulline and measured steady state incorporation of citrulline carbon into arginine and its precursor argininosuccinate by LC-MS (Fig. 4.2B). 100% of intracellular argininosuccinate and almost half of total intracellular arginine was

labeled by $^{13}C_5$-citrulline Fig. 4.2C,D). Thus, *de novo* synthesis contributes a substantial fraction of cellular arginine in TIFM cultured mPDAC cells. Consistent with this, inhibiting arginine synthesis by deprivation of citrulline and ornithine from TIFM results in a 10-fold decrease of intracellular arginine in mPDAC cells (Fig. 4.2E). This decrease in intracellular arginine is accompanied by a significant decrease in cell proliferation (Fig. 4.2F). Importantly, consistent with the consumption/release analysis by LC-MS (Fig. 4.2A), individual depletion of either citrulline or ornithine further shows that depletion of citrulline, but not ornithine, is the key substrate mPDAC cells require for arginine synthesis (Fig. 4.2G,H). To confirm the finding that *de novo* arginine synthesis is critical for mPDAC proliferation in TIFM, we used CRISPR-Cas9 to knockout (KO) *Ass1* in mPDAC cells (Fig. 4.2I). Consistent with decreased mPDAC proliferation upon *de novo* arginine synthesis inhibition by citrulline withdrawal, *Ass1* KO decreases mPDAC proliferation and this affect can be rescued by supplying additional exogenous arginine in TIFM or by re-expression of *Ass1* (Fig. 4.2J). Altogether, these findings suggest that *de novo* arginine synthesis is important to maintain intracellular arginine levels and mPDAC cell proliferation in TIFM.

Next, we asked if limited ability to synthesize arginine due to decreased Ass1 expression could explain the inability of mPDAC-RPMI cells to grow robustly in TIFM (Fig. 3.2). To test this, we first asked if increasing the arginine concentration in TIFM to 100μM could enable mPDAC-RPMI cells to grow in TIFM. We found arginine addition almost completely rescues the inhibition of cell growth observed when transferring mPDAC-RPMI cells directly to TIFM (Fig. 4.3). Thus, mPDAC-RPMI cells lose the ability to grow under arginine-deprived conditions, leading to their inability to grow in TIFM.

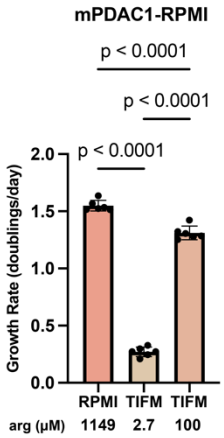

Figure 4.3. Arginine supplementation rescues cell proliferation defect of mPDAC1-RPMI cells in TIFM**.** mPDAC1-RPMI were cultured in TIFM, TIFM supplemented with 100uM arginine or in RPMI, as indicated. The proliferation rate of mPDAC1-RPMI cells immediately after switching the cells to the indicated media was measured (n=6). The values represent the mean and the error bars represent ± SD. Statistical significance was calculated using an ordinary one-way ANOVA test with Tukey's multiple comparison correction.

We next asked if arginine biosynthesis contributes to arginine homeostasis in murine PDAC tumors. To assess intratumoral PDAC arginine synthesis, we performed $^{15}N_2$-glutamine isotope tracing by multiple bolus intravenous injections of $^{15}N_2$-glutamine into mPDAC orthotopic tumor bearing mice and healthy controls (Fig. 4.4B). $^{15}N_2$-glutamine tracing can be used to monitor arginine synthesis and urea cycle activity in PDAC [115] by monitoring the incorporation of labeled glutamine derived nitrogen into arginine (Fig. 4.4A). After glutamine injection, healthy pancreas, tumor tissue, and plasma samples were collected, and ^{15}N enrichment in arginine and arginine biosynthetic precursors was measured by LC-MS. Glutamine in plasma is also quickly metabolized by multiple organs, which can then release labeled arginine and other metabolites into the circulation, which contribute to arginine labeling in other organs and the tumor [116]. One of the main examples of these interorgan exchange fluxes is the intestinal-renal axis, where glutamine metabolized by the small intestine is released as citrulline, which is then used by the kidneys to produce arginine for other tissues [116,117]. Consistent with systemic production of arginine from isotopically labeled glutamine, we observed an enrichment of ~14% $^{15}N_1$-arginine and ~7% $^{15}N_2$-arginine in the circulation of healthy and tumor bearing mice (Fig. 4.4C). For tissues whose sole

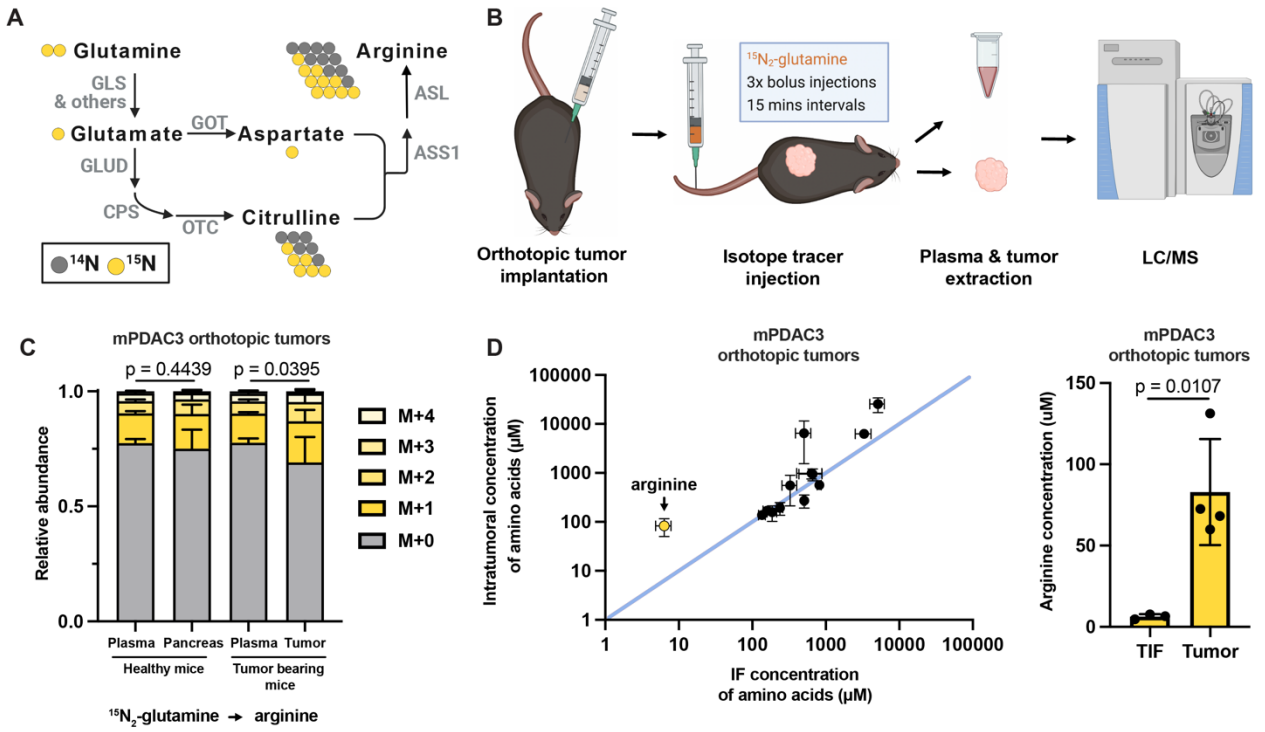

Figure 4.4. Arginine de novo synthesis is active in PDAC tumors. (A) Diagram showing the metabolic pathways mediating isotopic label incorporation from $^{15}N_2$-glutamine into arginine. (B) Diagram of stable isotope tracing by bolus intravenous injections of $^{15}N_2$-glutamine in orthotopic mPDAC3-TIFM tumor bearing mice and non-tumor-bearing controls followed by plasma sampling and tumor extraction for analysis of intratumoral metabolite labeling during the period of kinetic labeling. (C) Relative abundance of ^{15}N-labelled arginine isotopomers in tissues or plasma after $^{15}N_2$-glutamine tail-vein bolus injections (n=7). Statistical significance was calculated using a paired, one-tail student's t test. (D) (*left*) Concentrations of amino acids in IF (n=3) and tumor samples (n=4) of mPDAC3-RPMI orthotopic tumors measured by LC-MS. (*right*) Bar graph of intratumoral versus IF samples of arginine. For all panels, the bar graphs represent the mean and the error bars represent ± SD. Statistical significance was calculated using a two-tailed Student's t test.

source of arginine is uptake from the circulation, we expect the relative abundance of labeled arginine in the tissue would resemble that of the circulation. In line with this, the labeling pattern of arginine in non-ASS1 expressing healthy pancreas resembles the arginine labeling distribution found in circulation (Fig. 4.4C). In contrast, there is a greater amount of labeled arginine in PDAC tumor tissue compared to plasma, with ~17% $^{15}N_1$-arginine and ~9% $^{15}N_2$-arginine in tumors (Fig. 4.4C). While these non-steady state isotope labeling experiments cannot allow us to infer the fraction of intratumoral arginine that arises from *de novo* synthesis in PDAC tumors [118], the

appearance of additional ^{15}N enrichment in intratumoral arginine that cannot be explained by circulating labeled arginine confirms active synthesis of arginine in PDAC tumors, consistent with previous results that PDAC tumors highly express ASS1. Lastly, we compared the concentration of amino acids including arginine in the interstitial fluid of orthotopic murine PDAC tumors to the intratumoral arginine concentration (Fig. 4.4D). We observed that for most amino acids the intratumoral concentration was similar to the IF concentration. However, PDAC tumors had higher concentrations of free arginine than what is present in the TIF. Thus, we conclude that PDAC tumors accumulate higher levels of arginine than available from the local perfusate and that this is at least in part driven by *de novo* synthesis.

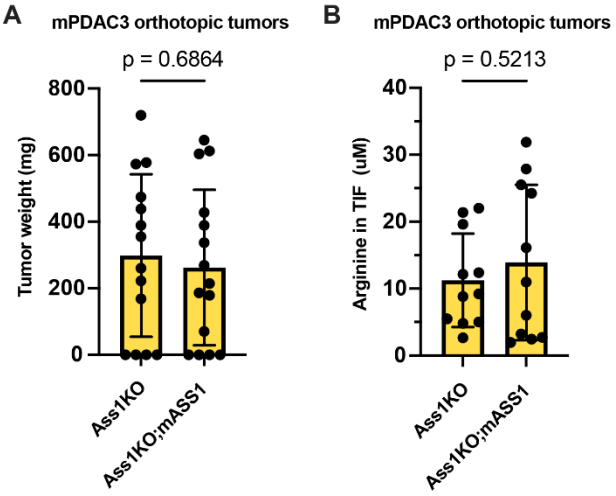

Figure 4.5. Inhibiting *de novo* arginine synthesis does not impair PDAC tumor progression. (A) Tumor weight of mPDAC3-TIFM-ASS1KO (n=14), and mPDAC3-TIFM-ASS1KO;mASS1 (n=15) orthotopic tumors. Statistical significance was calculated using a two-tailed Student's t test. (B) Arginine concentration in the TIF of mPDAC3-TIFM-ASS1KO (n=11), and mPDAC3-TIFM-ASS1KO;mASS1 (n=12) orthotopic tumors. Statistical significance was calculated using a two-tailed Student's t test.

Lastly, given the importance of *de novo* arginine synthesis for arginine homeostasis of both mPDAC cells in TIFM and in orthotopic tumors, we asked if inhibiting *de novo* synthesis would impair PDAC tumor growth as loss of this pathway impairs mPDAC cell growth in TIFM. To test this, we generated orthotopic PDAC tumors with mPDAC3-TIFM *Ass1* KO cells and control cells where *Ass1* was re-expressed (*Ass1*KO; mASS1). We found that loss of *Ass1* did not affect tumor growth despite low levels of arginine in the TME (Fig. 4.5A). These results suggest that, although arginine biosynthesis is active and upregulated in PDAC tumors (Fig. 4.1D, Fig. 4.4C), inhibiting this pathway is not detrimental for PDAC tumor growth.

4.3 Discussion

Use of the TIFM model uncovered arginine biosynthesis as a metabolic pathway that PDAC cells use under tumor microenvironmental nutrient conditions. Arginine biosynthesis is a metabolically costly process due to the utilization of aspartate, leading to silencing of ASS1 in many tumor types [108]. Because of this, the finding of PDAC cells synthesizing arginine was initially surprising. Why would this tumor suppressive metabolic pathway be activated in PDAC?

Multiple studies have also shown that cancer cells reactivate ASS1 expression and arginine biosynthesis when extracellular arginine becomes limited to support tumor growth. For example, ASS1-silenced tumors treated with arginine deiminase to eliminate extracellular arginine acquire resistance to such therapy by reactivating ASS1 expression [119,120]. In another example, reactivation of arginine biosynthesis was shown to be necessary to support metastasis of clear cell renal cancers to the arginine limited lung environment, whereas arginine biosynthesis was not necessary and inactive in the arginine-replete primary tumor [45]. Lastly, ATF4-CEBPβ mediated upregulation of ASS1 upon amino acid stress has been shown to allow AML cells to adapt to low levels of microenvironmental arginine [121]. Altogether, these findings suggest that the tumor suppressive role of arginine biosynthesis is context dependent. In the context of microenvironmental arginine deprivation, ASS1 and arginine biosynthesis can switch their role to become tumor supportive. One of the most depleted nutrients in the PDAC TME is the amino acid arginine, which we previously observed was depleted ~20-50 fold from circulatory concentrations to only 2-5μM [40]. Thus, we initially hypothesized that: (1) arginine deprivation in the PDAC TME would activate arginine biosynthesis, which (2) would be tumor promoting rather than tumor suppressive by enabling PDAC cells to maintain cellular arginine levels despite TME constraints.

However, our results suggest that the above model of arginine synthesis regulation and homeostasis in PDAC is far from complete. Both in TIFM and *in vivo*, we found that PDAC cells synthesize arginine (Fig 1M-N, Fig 2D-E & K), and that arginine synthesis is critical for PDAC arginine homeostasis and growth in TIFM (Fig 2F-H). However, this pathway is dispensable for PDAC growth *in vivo* (Fig 2 – Figure supplement 3). Thus, PDAC tumors *in vivo* can adapt to loss of this pathway while PDAC cells in TIFM cannot. It remains unclear how PDAC tumors metabolically compensate for loss of arginine synthesis. We speculate that this is possible through a variety of mechanisms that involve upregulation of alternative pathways to obtain arginine and or support from other components of the tumor microenvironment, both of which are discussed at length in Chapter 5.

CHAPTER 5

ENHANCED UPTAKE OF ENVIRONMENTAL ARGININE ALLOWS PDAC CELLS TO COPE WITH INHIBITION OF DE NOVO ARGININE SYNTHESIS

5.1 Introduction

The data presented in Chapter 4 of this thesis shows that under TME nutrient stress, PDAC cells require de novo arginine synthesis for maximal growth. Nevertheless, inhibiting arginine synthesis, either genetically or by starvation of precursors for this pathway (citrulline and ornithine) does not completely inhibit PDAC growth in TIFM, and PDAC tumor growth is not significantly impaired by inhibition of this pathway. This suggests that PDAC cells can adapt to survive and grow in the face of not only arginine starvation but inhibition of de novo synthesis as well. How do PDAC cells adapt? We hypothesized that PDAC cells must compensate with other mechanisms to acquire arginine when synthesis is inhibited. In addition to *de novo* synthesis, there are two other known pathways for arginine acquisition by PDAC cells: macropinocytosis, the nonselective uptake of extracellular fluid and material, [122] and cationic amino acid transporter mediated uptake [110] (Fig. 5.1).

Previous studies have reported that Kras-driven PDAC cancer cells upregulate macropinocytosis[123]. Increase of micropinocytosis in PDAC is enabled by Kras-mediated regulation of transmembrane glycoprotein SDC1[124,125]. Thus, macropinocytic uptake and lysosomal breakdown of extracellular protein has been postulated as a source of amino acids for PDAC tumors[82,123,124]. Similarly, multiple tumors types have been previously reported to

preferentially upregulate extracellular arginine uptake to maintain arginine homeostasis after silencing of *de novo* arginine biosynthesis[108,126]. With this in mind, we wanted to test whether either or a combination of these pathways supports PDAC cell growth after inhibition of arginine

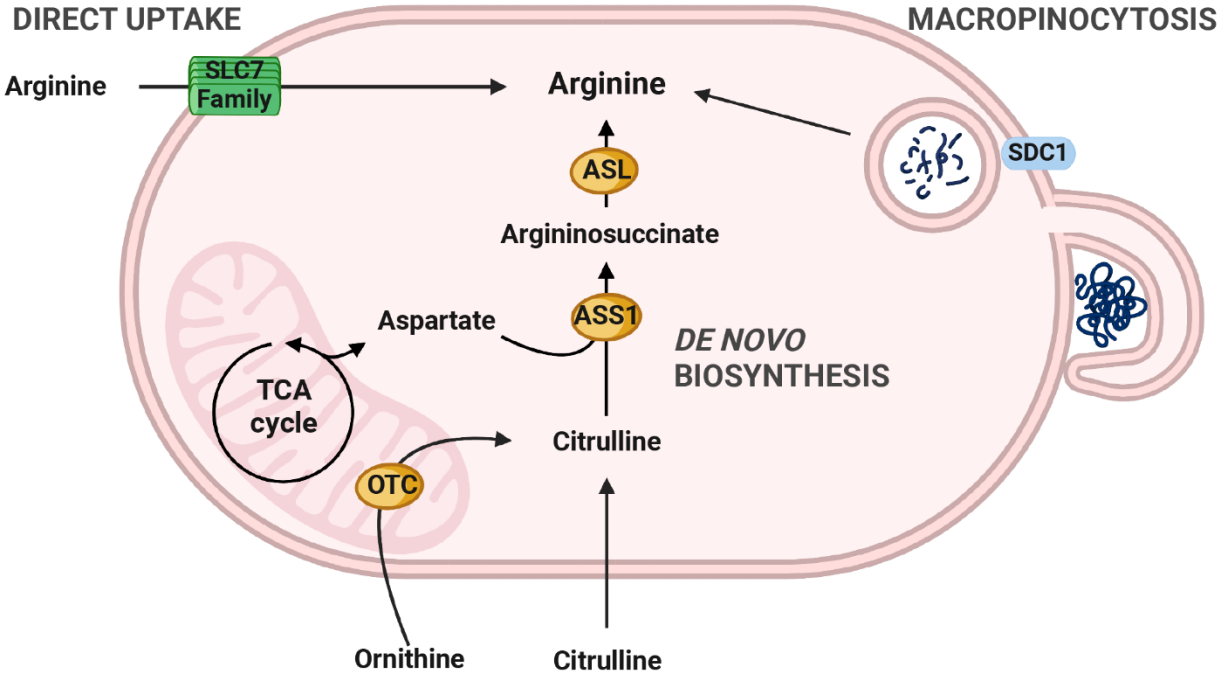

Figure 5.1. Three cellular pathways to obtain arginine. Cells can acquire arginine by either of three routes: direct uptake of free arginine from the microenvironment, *de novo* synthesis and uptake and breakdown of extracellular protein (macropinocytosis).

de novo synthesis.

5.2 Results

To test if macropinocytosis is important for arginine homeostasis in mPDAC cells in TIFM, we generated mPDAC1-TIFM cells with a doxycycline-inducible shRNA targeting glycoprotein syndecan-1 (SDC1), an important mediator of macropinocytosis in PDAC cells [124] (Fig. 5.2A). Knockdown of *Sdc1* effectively reduced mPDAC1-TIFM macropinocytosis rate as measured by uptake and catabolism of fluorogenic bovine serum albumin (DQ-BSA), a model

macropinocytosis substrate (Fig. 5.2B). *Sdc1* knockdown did not affect intracellular arginine pools nor cell proliferation in TIFM cultured mPDAC cells (Fig. 5.2C,D). Consistent with this, pharmacological inhibition of lysosomal protein breakdown with hydroxychloroquine (HQ) similarly impairs mPDAC1-TIFM macropinocytosis rate without disrupting cell proliferation (Fig. 5.2E,F). Furthermore, knockdown of *Sdc1* did not further impair mPDAC cell proliferation upon inhibition of arginine synthesis (Fig. 5.2G), suggesting macropinocytosis is also not critical for mPDAC cells upon inhibition of *de novo* arginine synthesis. Thus, we conclude that macropinocytosis does not contribute to mPDAC arginine homeostasis in TIFM, even as an adaptive mechanism upon *de novo* arginine synthesis inhibition.

We next tested if uptake of the small amount of free arginine in TIFM (~2μM) mediates the ability of mPDAC cells to cope with inhibition of *de novo* arginine synthesis. In normal TIFM culture, removal of arginine does not affect mPDAC intracellular arginine levels nor proliferative capacity (Fig. 5.3A,B). Thus, as with macropinocytosis, arginine uptake is not critical for mPDAC arginine homeostasis in TIFM conditions. We next tested if depriving mPDAC cells of the

Figure 5.2. (following page) mPDAC cells do not upregulate macropinocytosis after inhibition of arginine synthesis. (A) RTqPCR analysis for *Sdc1* in mPDAC1-TIFM cells infected with lentiviruses encoding a dox inducible *Sdc1* targeting shRNA or *Renilla* luciferase targeting control shRNA (shRen) with and without treatment with 1 μg/mL doxycycline or vehicle (n=6). (B) Macropinocytosis activity measured by kinetic DQ-BSA uptake assay in mPDAC1-TIFM cells from (A). (C) Relative intracellular arginine levels of mPDAC1-TIFM cells infected with lentiviruses encoding a doxycycline inducible *Sdc1* targeting shRNA or a *Renilla* luciferase targeting control shRNA (shRen) treated with 1 μg/mL doxycycline or vehicle (n=6). (D) Cell proliferation rate of mPDAC1-TIFM cells in same conditions as (A) (n=6). (E) Macropinocytosis activity measured by kinetic DQ-BSA uptake in mPDAC1-TIFM cells treated with 10μM hydroxychloroquine (HQ) or vehicle (water). (F) Cell proliferation rate of mPDAC1-TIFM cells in same conditions as (E) (n=3). (G) Proliferation rate of mPDAC1-TIFM cells as in (A) cultured in TIFM with or without citrulline (cit) and ornithine (orn) (n=5). For all panels, bar graphs represent the mean, and the error bars represent ± SD. Statistical significance for panels B and E was calculated using an ordinary one-way ANOVA test with Tukey's multiple comparison correction. For panels A, C, D, F and G statistical significance was calculated using a two-tailed Student's t test.

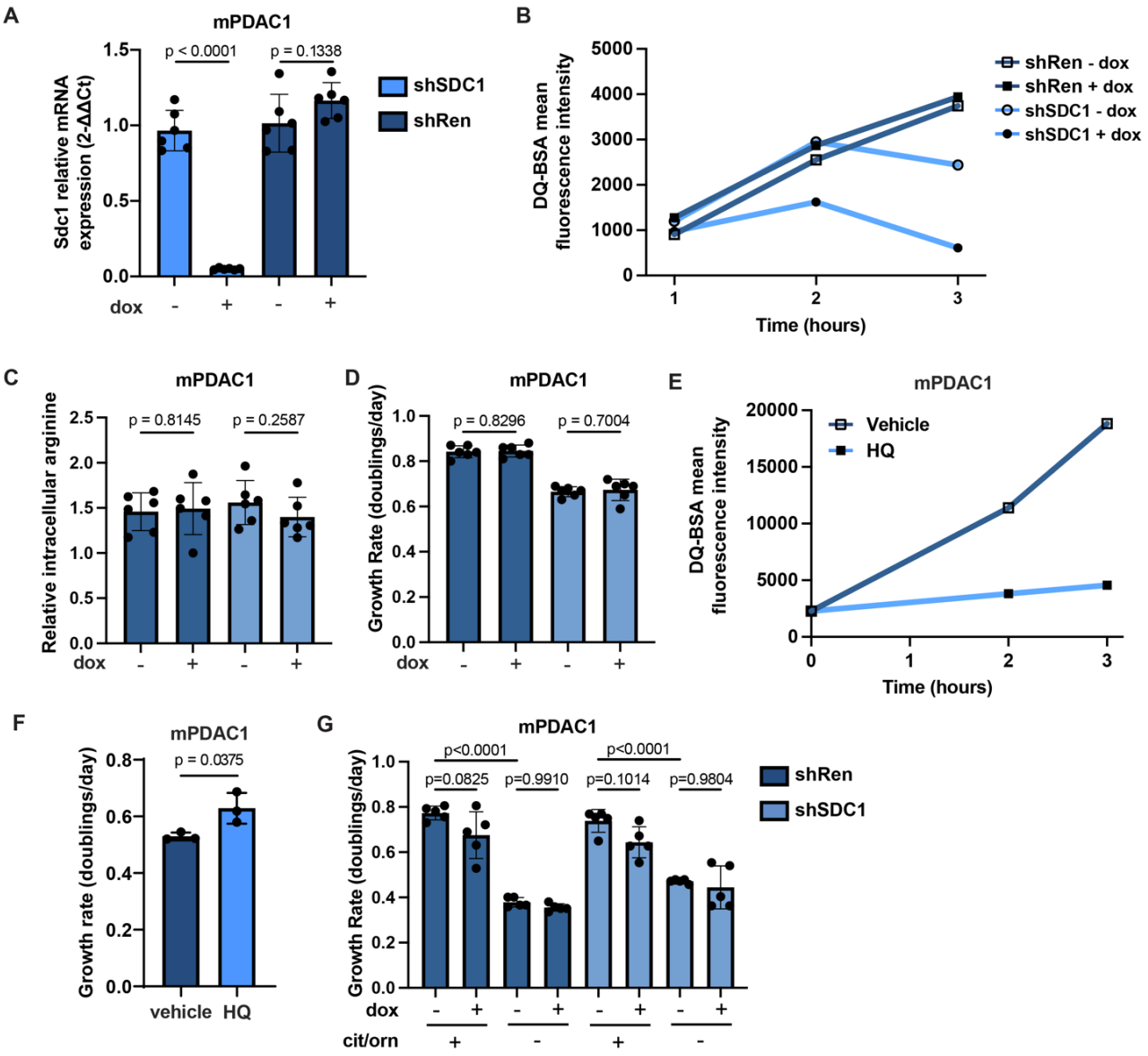

available microenvironmental arginine after *de novo* biosynthesis is impaired would affect mPDAC arginine homeostasis and growth. We found that inhibition of arginine synthesis in TIFM cultured mPDAC cells leads to increased transcription of arginine transporters (Figure 5.3C) and leads to an increased rate of arginine uptake by mPDAC cells (Fig. 5.3D). Furthermore, while we could not detect decreases in mPDAC intracellular arginine levels after eliminating extracellular arginine (Fig. 5.3E), eliminating TIFM extracellular arginine completely abrogates cell growth in of mPDAC cells upon inhibition *of de* novo arginine synthesis (Fig. 5.3F). Altogether, these data

suggest that mPDAC cells upregulate extracellular arginine uptake to cope with inhibition of arginine biosynthesis and that this could be in part mediated by the upregulation of cationic amino acid transporters.

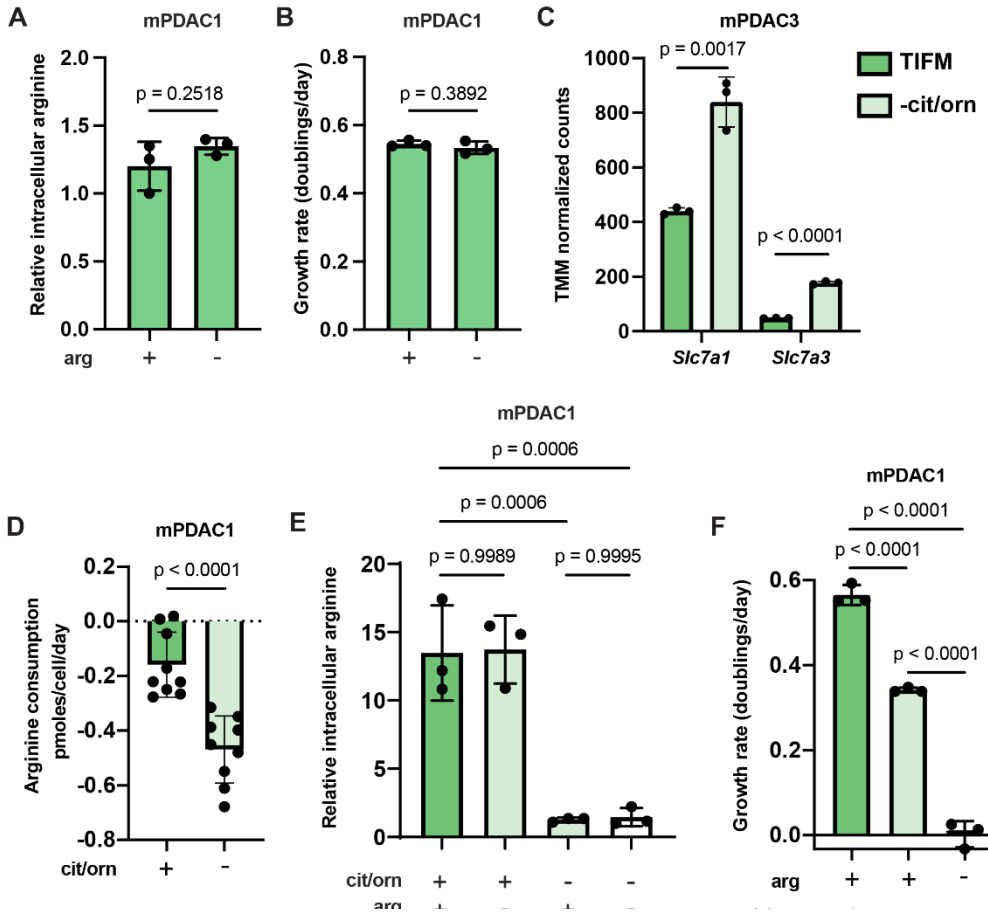

Figure 5.3. Enhanced uptake of environmental arginine allows PDAC cells to cope with inhibition of de novo arginine synthesis. (A) Relative intracellular arginine levels of mPDAC1-TIFM cells grown in TIFM with or without TIFM concentrations of arginine (arg) (n=3). (B) Cell proliferation rate of mPDAC1-TIFM cells in same conditions as (A) (n=3). (C) Trimmed mean of M values (TMM)-normalized counts for *Slc7a1* and *Slc7a3,* two cationic amino acid transporters capable of transporting arginine, from transcriptomic analysis of mPDAC3-TIFM cells grown in either TIFM or TIFM without citrulline and ornithine (n=3). (D) Per-cell consumption rate of arginine by mPDAC1-TIFM cells cultured in TIFM with or without citrulline and ornithine. Cells were supplemented with 20μM arginine to enable the consumption measurements (n=9). (E) Relative intracellular arginine levels of mPDAC1-TIFM cells grown in TIFM with or without PDAC IF concentrations of citrulline, ornithine, or arginine, as indicated (n=3). (F) Proliferation rate of mPDAC1-TIFM cells grown with or without TIFM concentrations of citrulline, ornithine, or arginine, as indicated (n=3). For all panels, bar graphs represent the mean, and the error bars represent ± SD and statistical and G statistical significance was calculated using a two-tailed Student's t test.

5.3 Discussion

Using TIFM, we have identified compensatory arginine uptake upon synthesis inhibition (Fig 5.3). Arginine uptake could not fully compensate for the lack of arginine synthesis but still allowed PDAC cells to survive and grow at diminished rates. Given that inhibition of arginine biosynthesis does not affect PDAC tumor growth (Fig 4.5), it is possible that, *in vivo,* arginine uptake is further enhanced or is otherwise sufficient to enable PDAC tumors to grow unperturbed. In TIFM, we did not identify a role for macropinocytosis in arginine acquisition or maintaining PDAC viability and growth (Fig 3A-C).

This is in contrast to other studies that have identified a role for macropinocytosis in PDAC amino acid acquisition and tumor progression [123,124,127,128]. However, other TME factors not included in the TIFM model such as hypoxia, activate macropinocytosis and render it more essential [129]. Thus, macropinocytosis could play a more active role in maintaining arginine homeostasis and PDAC growth *in vivo*, enabling PDAC tumors to compensate for the lack of arginine synthesis.

Lastly, the TIFM model lacks stromal cells, which have been shown to exchange macromolecules and nutrients with cancer cells [130,131]. Stromal-cancer cell metabolic exchange in vivo could potentially buffer the lack of arginine synthesis. More analysis will be required to understand the metabolic mechanisms that PDAC uses to maintain arginine homeostasis in the TME.

CHAPTER 6

MYELOID ARGINASE CAUSES LOCAL ARGININE DEPLETION IN PDAC

6.1 Introduction

PDAC tumors are characterized by extensive infiltration of immune cells, with macrophages being one of the most prominent immune cell populations among the PDAC tumor stroma [132,133], including many arginase-1-expressing cells [134]. Myeloid cell mediated arginase activity in solid tumors has been particularly studied as a hallmark of an alternatively activated, tumor promoting macrophage state, usually denoted as M2, mainly in the context of immune suppression. Our previous work has shown that arginine levels in the TIF are strikingly low[40]. We have also observed that levels of ornithine, a product of arginine catabolism by arginase, are higher in PDAC TIF relative to plasma, suggesting that arginase might play a role in the depletion of arginine in the microenvironment.

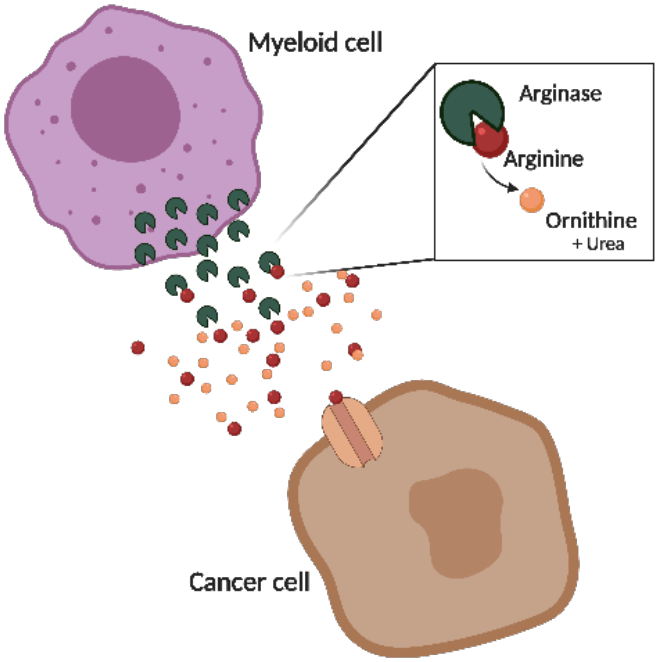

Figure 6.1. Proposed model for arginine depletion in PDAC TIF. Myeloid cells release arginase into the extracellular environment, catabolizing it into ornithine and impeding uptake by adjacent cells.

Such a scenario of local nutrient availability in the TME being directly influenced by myeloid cells would fit a growing trend of stromal regulation of tumor metabolism. Indeed, recent studies have reported on the role of stromal cells in regulating nutrient availability in tumors. Fibroblasts, for example, influence the levels of various metabolites in the TME [135], including amino acids [131,136] and lipids [137]. More notably, myeloid cells have been shown to be the major glucose-consuming cell type in multiple tumor types [51]. Thus, myeloid cells are important regulators of nutrient availability in the TME. With this in mind, we wanted to test whether myeloid derived arginase activity could be responsible for the low levels of arginine in the PDAC TME.

6.2 Results

We confirmed the presence of a robust myeloid and arginase-1 expressing population in both murine (Fig. 6.2A) and human PDAC (Fig. 6.2B) by immunohistochemical analysis. Arginase-1 expressing cells are capable of metabolizing arginine into ornithine and urea [138]. Therefore, we

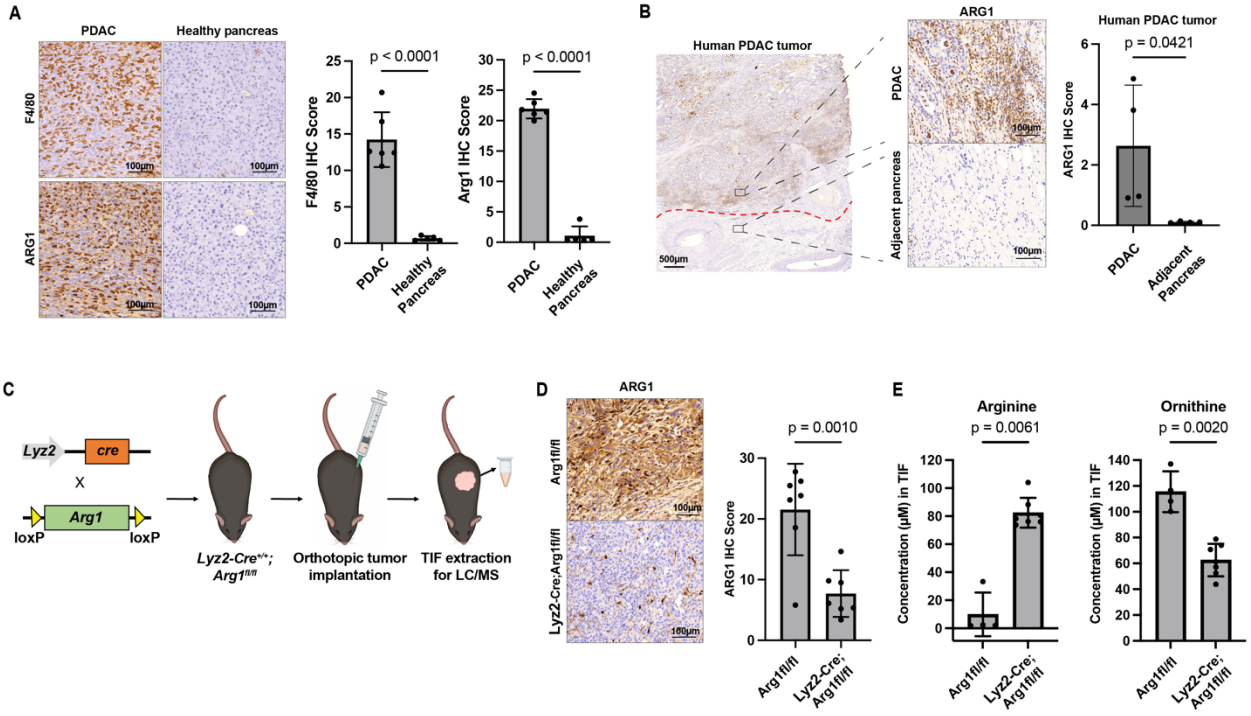

Figure 6.2. (previous page) Myeloid arginase causes microenvironmental arginine depletion in PDAC tumors. (A) Representative images (left) and IHC score (right) of immunohistochemical (IHC) staining for F4/80 and ARG1 in an orthotopic mPDAC1-TIFM tumor (n=5) and in healthy murine pancreas (n=5). Scale bars: 100µm. Multiple regions of malignant tissue for each sample were used to assess staining and the same annotated regions for F4/80 were utilized to assess ARG1 expression. (B) Representative images (*left*) and IHC score (*right*) of IHC staining for ARG1 in an advanced human PDAC tumors and adjacent untransformed pancreas (n=4). Multiple regions with myeloid cells for untransformed pancreas and for PDAC tumors for were used for this analysis. Scale bar: 500µm and 100µm, as indicated. (C) Schematic for crossing of *Lyz2-Cre* and $Arg1^{fl/fl}$, tumor implantation in $Lyz2\text{-}Cre^{+/+}$; $Arg1^{fl/fl}$ progeny and subsequent IF extraction. (D) Representative images (*left*) and IHC score (*right*) of IHC staining for ARG1 protein expression in orthotopic mPDAC3-TIFM tumors from $Lyz2\text{-}Cre^{+/+}$; $Arg1^{fl/fl}$ (n=7) and $Arg1^{fl/fl}$ littermate controls (n=7). Scale bar: 100µm. Multiple regions of malignant tissue for each sample were used to assess ARG1 staining. (E) Absolute concentration of arginine and ornithine in the IF of orthotopic mPDAC3-TIFM tumors from $Lyz2\text{-}Cre^{+/+}$; $Arg1^{fl/fl}$ (n=7) and $Arg1^{fl/fl}$ littermate controls (n=4). Statistical significance for all figures was calculated using a two-tailed Student's t test.

hypothesized that myeloid arginase-1 activity could be responsible for PDAC TME arginine starvation. To test this, we generated orthotopic allograft mPDAC tumors in a mouse model with myeloid specific *Arg1* knockout ($Lyz2\text{-}Cre^{+/+}$; $Arg1^{fl/fl}$) [139,140] and control animals $Arg1^{fl/fl}$). We then isolated IF from these tumors at end-stage and measured the levels of amino acids, including arginine and ornithine in these samples (Fig. 6.2C). Compared to control animals, $Lyz2\text{-}Cre^{+/+}$; $Arg1^{fl/fl}$ tumors show robust reduction of arginase-1 expression in tumors (Fig. 6.2D) confirming most arginase-1 in tumors is myeloid in origin. $Lyz2\text{-}Cre^{+/+}$; $Arg1^{fl/fl}$ tumors had ~9-

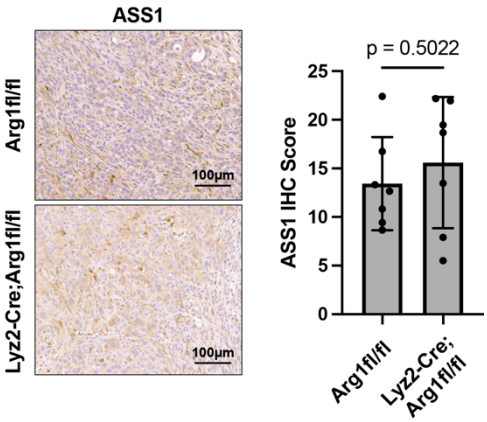

Figure 6.3. mPDAC tumors in Lyz2-Cre$^{+/+}$; Arg1$^{fl/fl}$ mice and controls show no difference in ASS1 expression. Representative images (*left*) and IHC score (*right*) of IHC staining for ASS1 protein expression in orthotopic mPDAC3-TIFM tumors from *Lyz2-Cre*$^{+/+}$; *Arg1*$^{fl/fl}$ (n=7) and *Arg1*$^{fl/fl}$ littermate controls (n=7). Multiple regions of malignant tissue for each sample were used to assess ASS1 staining. Statistical significance for all figures was calculated using a two-tailed Student's t test.

fold increase in IF arginine concentration and a roughly equimolar decrease in ornithine (Fig. 6.2E). Pharmacological inhibition of arginase-1 with the small-molecule inhibitor CB-1158 [79] in mPDAC orthotopic tumors also led to an increase in IF arginine compared to control tumors (Fig. 6.3). In summary, these results show that arginase activity in the myeloid compartment of PDAC tumors is responsible for arginine depletion in the TME.

ASS1 expression is known to be tightly regulated in cancer cells. ASS1 expression in some cancer cells is silenced when exogenous arginine is available, as arginine synthesis can otherwise slow the proliferation of cancer cells [107]. Therefore, we asked if arginine synthesis is always active in PDAC tumors, or this pathway adaptively responds to TME arginine levels. To ask this, we assessed arginine biosynthesis in PDAC tumors in *Lyz2-Cre*$^{+/+}$*; Arg1*$^{fl/fl}$ (high TME arginine) compared to *Arg1*$^{fl/fl}$ control (low TME arginine) host animals. We first assessed expression of

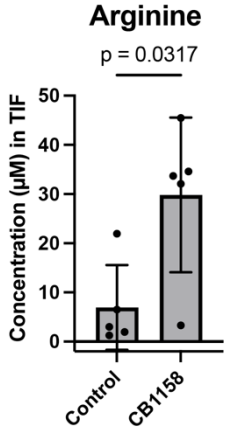

Figure 6.4. Treatment with arginase inhibitor CB-1158 increases arginine levels in mPDAC tumor TIF. Absolute concentration of arginine in the IF of mPDAC3-TIFM orthotopic tumors after treatment with 100mg/kg of arginase inhibitor CB-1158 or vehicle (n=5). Statistical significance was calculated using a two-tailed Student's t test.

ASS1 and found no difference in PDAC cell expression of ASS1 between *Lyz2-Cre*$^{+/+}$*; Arg1*$^{fl/fl}$ and control tumors (Fig. 6.4). Further, we assessed arginine synthesis by continuous infusion of $^{15}N_2$-glutamine in PDAC bearing *Lyz2-Cre*$^{+/+}$*; Arg1*$^{fl/fl}$ and control animals [115]. We did not observe significant differences in labeling of tumor argininosuccinate or arginine (Fig. 6.5), from which we conclude arginine synthesis is similarly active in PDAC tumors with arginine starved and replete TMEs. Altogether, this data suggests arginine synthesis is constitutively active in PDAC tumors and does not respond to TME arginine availability.

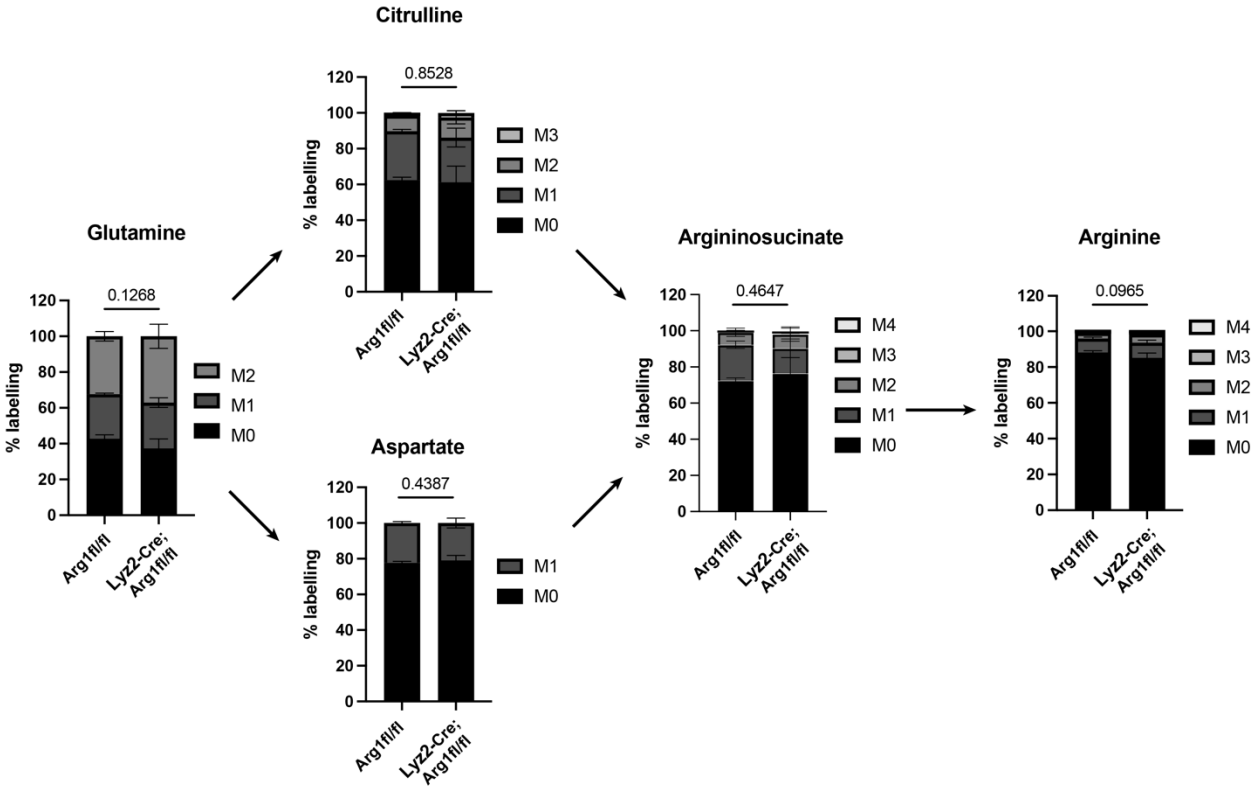

Figure 6.5. $^{15}N_2$-glutamine tracing in *Lyz2-Cre*$^{+/+}$*; Arg1*$^{fl/fl}$, mPDAC3-TIFM tumor bearing mice does not show reduction of arginine biosynthesis. Mass isotopomer distributions of glutamine, citrulline, aspartate, argininosuccinate and arginine in mPDAC3 tumors in *Lyz2-Cre*$^{+/+}$*; Arg1*$^{fl/fl}$ (n=9) and *Arg1*$^{fl/fl}$ (n=3) hosts after $^{15}N_2$-glutamine infusion. Statistical significance was calculated using a paired, two-tailed student's t test.

6.2 Discussion

We previously found that the TME is arginine depleted [40]. However, what drove arginine depletion in the TME was unknown. Here, we find that the arginase-1 expressing myeloid compartment in PDAC tumors is largely responsible for TME arginine depletion (Fig. 4). Consistent with these findings, Menjivar and colleagues also found PDAC associated myeloid cells are critical for mediating TME arginine depletion [141]. Thus, the most striking nutrient perturbation in the TME is not driven by abnormal cancer cell metabolism, but is instead driven by stromal metabolic activity. This finding aligns with recent studies documenting the critical role of stromal cells in influencing nutrient availability in the TME. For example, in addition to the role we have found for myeloid cells in limiting TME arginine, myeloid cells were also found to be the major glucose consuming cell type in a variety of tumor types [51].

Thus, stromal myeloid cells may be key regulators of glucose availability in the TME. Fibroblasts have been shown to also regulate levels of key metabolites in the TME [135], such as amino acids [131,136] and lipids [137]. In addition, tumor innervating neurons were also shown to regulate availability of amino acids in the TME [142]. Thus, future studies delineating the complex metabolic interactions amongst tumor and stromal cells [5] will be critical to understanding how nutrient availability is regulated in the tumor ecosystem and how the resulting nutrient milieu impacts cancer and stromal cell metabolism and biology.

CHAPTER 7

SIGNIFICANCE AND FUTURE DIRECTIONS

7.1 Significance

Pancreatic ductal adenocarcinoma (PDAC) is a very aggressive, yet initially asymptomatic cancer that is usually diagnosed at a late stage, at which point the 5-year-survival rate is as low as 3%[143]. The aggressive biology of PDAC and current lack of effective treatment modalities underscore the need for novel therapeutic targets against this disease[31].PDAC is characterized by high levels of desmoplastic growth that result in a hypovascularized, poorly perfused tumor. The prominence of desmoplastic stromal cells and dysfunctional vasculature in PDAC have been shown to reduce the levels of available oxygen in the tumor microenvironment (TME)[144,145], and we hypothesized that these same pathophysiological conditions result in an altered nutrient microenvironment beyond oxygen availability. Indeed, we have seen that nutrient availability in PDAC tumors is very different from that of circulation. With this work, we have further show that this altered nutrient microenvironment in turn affects biological proceses including but not limited to the metabolism cancer cells. The study and discovery of similar adaptations as the ones presented in this thesis will give us a better understanding of how PDAC cell biology enables disease progression, and thus get us closer to finding novel targets against PDAC.

The need to develop more efficient targeted therapeutics is echoed for the treatment of multiple, aggressive cancer types. While efforts to target the metabolism of cancer cells have historically approached this by trying to uncover genetically driven changes in metabolic processes, growing evidence suggests that the environment cancer cells reside in can also affect therapy[83]. We have shown that tumor type, anatomical location and diet can all affect the

availability of nutrients in the TME[40]. Therefore, it is logical to assume that different tumor types, in different parts of the body, will not exhibit the same metabolic adaptations as PDAC cells exhibit in TIFM and their TME Thus, the use of TIFM may not directly be extended to study the metabolic adaptations of other tumor types. However, the methodology used in this thesis of measuring TME nutrient levels and developing media representing those conditions is not limited to studying PDAC, and the same workflow can be applied to a variety of cancers. Thus, the approaches I developed, have potential applications well beyond the scope of pancreatic cancer.

The TME is a potent regulator of cell state and function. The TME impacts every type of cell present in a tumor. Malignant cells[146,147], macrophages[148,149], fibroblasts[150], and T cells[48,49] have all been documented to be heavily influenced by TME cues. TME influence of these different tumor resident cell populations can substantially impact tumor progression and clinical outcomes. For example, the TME has been linked to aggressive features of cancer cells such as chemoresistance[151,152] and metastatic behavior[153,154]. TME-stromal cell interactions also contribute to tumor progression. For example, tumor-associated macrophages adopt a pro-tumorigenic cell state intimately linked to the TME[155]. In another example, tumor-infiltrating T-cells are driven to a dysfunctional cell state by the TME, which allows for immune evasion and disease progression [156]. Thus, interactions between multiple cell types resident in tumors and the TME are critical drivers of many aspects of tumor biology. Therefore, knowledge of the composition of the TME and how this interacts with various tumor resident cells will be essential to improve our understanding of tumor biology.

7.2 Future Directions

7.2.1 The use of TIF-based analyses and the use of physiological media

Cell-based models remain critical tools for mechanistic discovery and therapeutic target identification in cancer biology. However, many biological findings and drug targets that arise from these cell-based studies fail to translate to cancer cells *in vivo* or in clinical settings [58]. That cancer cells behave so differently in *in vitro* culture systems than when growing in tumors suggests that cancer cell behavior is not only cell-intrinsically encoded. Rather, cell-extrinsic cues in the TME are capable of dramatically influencing the cancer cell state and impacting many aspects of cancer cell biology, including therapy response [152]. The importance of TME cues in regulating cancer cell behavior has prompted new efforts to develop cell-based models that incorporate key microenvironmental influences to both improve their disease relevance and fidelity [58] and enable mechanistic studies delineating how the microenvironment influences cancer cell biology.

Here, we have shown that growing PDAC cells in physiological nutrition caused substantial transcriptional reprogramming, moving PDAC cells towards a more *in vivo*-like transcriptional state compared to non-physiological standard culture conditions. Furthermore, incorporating other aspects of the TME with TIFM could further expand our ability to understand cancer cell metabolism using this modeling system. Indeed, components of the TME that are not intrinsically a part of TIFM, such as hypoxia, other cell populations, extracellular matrix, and others have been proposed to support the metabolic adaptation of cancer cells to nutrient stress, including arginine deprivation [129]. A notable example is the recent discovery that PDAC tumor hypoxia activates macropinocytosis *in vivo,* an adaptation that we do not observe using TIFM [129]. Thus, building

upon TIFM by modeling tumor oxygen levels could potentially lead to the discovery of other physiologically relevant PDAC metabolic adaptations. Our results not only underscore the key role of nutrient TME in regulating cancer cell metabolism and biology but also illustrate the potential of modeling the TME and building upon tools such as TIFM.

The development of easily deployable techniques to isolate TIF and modern analytical technologies to characterize the composition of these isolates has led to a wealth of new information on the composition of the TME. This new understanding of TIF composition has already contributed to our knowledge of how the TME triggers key cell biological phenotypes that affect disease pathology. Thus, TIF analysis will play a key role in unraveling how the TME regulates tumor biology. We anticipate the following future developments will maximize our ability to learn about how the TME regulates tumor biology from TIF analysis.

First, multi-analytical characterization of samples to completely characterize TIF composition will improve our understanding of the TME. Currently, most TIF analysis studies have focused on reporting the electrolyte, metabolite, or protein content of TIF from different tumors individually. However, these components of TIF play interrelated roles in regulating the biology of tumor resident cells. Thus, a more complete characterization of TIF will be necessary to uncover how these different molecular components of TIF interact collectively to regulate tumor cell biology.

Second, while measurements of TIF composition provide information on the content of the TME, it is currently a challenge to determine which of the identified TIF components regulate tumor resident cells. By analogy with another TME component, while single cell analysis technologies can measure the cellular content of tumors[15], this does not indicate how different cell types in tumors impact cell and tumor biology. The development of techniques such as ligand-

receptor pairing of cell types in the TME has been critical in determining how the cellular composition of the TME functionally regulates different cell types[16]. Similarly, our ability to measure the composition of TIF outstrips our ability to determine how TIF components regulate tumor cell biology. Thus, new experimental tools that enable systematic assessment of how TIF components regulate tumor cell biology will improve our ability to use TIF analysis to understand TME biology. Approaches such as developing model systems where cells can be cultured while exposed to TIF-mimicking media[41] may be one such technical advance enabling the identification of the TIF-cell interactions that are functionally critical for how the TME impacts tumor biology. However, further advances in this area will be necessary to translate our increasing knowledge of TIF composition into an understanding of how this key component of the TME influences tumor biology.

7.2.2 Arginine deprivation in the tumor microenvironment

We initially hypothesized that: (1) arginine deprivation in the PDAC TME would activate arginine biosynthesis, which (2) would be tumor promoting rather than tumor suppressive by enabling PDAC cells to maintain cellular arginine levels despite TME constraints. However, our results suggest that the above model of arginine synthesis regulation and homeostasis in PDAC is far from complete. First, arginine deprivation is not the sole microenvironmental signal that leads to upregulation of arginine synthesis in PDAC tumors. Raising TME arginine levels by inhibiting myeloid arginase expression does not appear to modulate ASS1 expression or tumor arginine synthesis. This strongly suggests that other TME cues aside from arginine deprivation drive expression of the arginine synthesis pathway. The fact that cells cultured in TIFM maintain expression of the arginine synthesis pathway suggests that other nutrient cue(s) may regulate

expression of arginine synthesis genes. More work will be required to understand the TME cues that lead to arginine synthesis *in vivo*.

Second, in TIFM and *in vivo*, we found that PDAC cells synthesize arginine, and that arginine synthesis is critical for PDAC arginine homeostasis and growth in TIFM. However, this pathway is dispensable for PDAC growth *in vivo*. Thus, PDAC tumors *in vivo* can adapt to loss of this pathway while PDAC cells in TIFM cannot. It remains unclear how PDAC tumors metabolically compensate for loss of arginine synthesis. We speculate PDAC tumors could adapt to arginine synthesis inhibition by a combination of compensatory arginine uptake, as identified in TIFM, and other TME factors not included in the TIFM model such as hypoxia [129], as discussed in detail in Chapter 4. More analysis will be required to understand the metabolic mechanisms that PDAC uses to maintain arginine homeostasis in the TME.

The lack of arginine in the TME can further have major impacts on stromal cells that may not have the adaptive capabilities of PDAC cells. For example, anti-tumor lymphocytes require arginine for functionality [157], but are not able to upregulate arginine biosynthesis upon arginine starvation [121]. Thus, microenvironmental arginine availability is known to limit immune responses in a variety of tumor types [158]. This has led to many recent efforts to develop pharmacological tools to increase TME arginine [79,159], which have improved immunotherapeutic outcomes in a variety of murine tumor models [79,159–161]. Thus, the severe arginine restriction in the PDAC TME could be a major barrier to immunotherapy in this disease, which is refractory to most immunotherapies [162]. Consistent with this hypothesis, low arginine availability does impair anti-tumor immunity in PDAC and raising TME arginine levels can improve tumor immune surveillance and response to immunotherapy [141,163]. Thus, arginine starvation is a key nutrient limitation that both PDAC and stromal cells face in the TME. *De novo*

arginine synthesis and other adaptive mechanisms PDAC cells allow cancer cells to cope with such arginine starvation. However, other cell types without such adaptive capacity, such as lymphocytes, face dysfunction in the arginine deprived TME. Future studies delineating how different cellular populations are affected by TME arginine starvation will prove critical to better understanding how tumor physiology impacts cancer and stromal cell biology.

REFERENCES

1. Hanahan D, Weinberg RA. Hallmarks of cancer: The next generation. Cell. 2011;144: 646–674.

2. Hanahan D. Hallmarks of Cancer: New Dimensions. Cancer Discov. 2022;12: 31–46.

3. Lau AN, Vander Heiden MG. Metabolism in the tumor microenvironment. Annu Rev Cancer Biol. 2020;4: 17–40.

4. Faubert B, Solmonson A, DeBerardinis RJ. Metabolic reprogramming and cancer progression. Science. 2020;368: eaaw5473.

5. Li F, Simon MC. Cancer Cells Don't Live Alone: Metabolic Communication within Tumor Microenvironments. Dev Cell. 2020;54: 183–195.

6. DeBerardinis RJ, Chandel NS. Fundamentals of cancer metabolism. Sci Adv. 2016;2: e1600200.

7. Vander Heiden MG, DeBerardinis RJ. Understanding the Intersections between Metabolism and Cancer Biology. Cell. 2017;168: 657–669.

8. Bi J, Wu S, Zhang W, Mischel PS. Targeting cancer's metabolic co-dependencies: A landscape shaped by genotype and tissue context. Biochim Biophys Acta Rev Cancer. 2018;1870: 76–87.

9. Nagarajan A, Malvi P, Wajapeyee N. Oncogene-directed alterations in cancer cell metabolism. Trends Cancer. 2016;2: 365–377.

10. Altea-Manzano P, Cuadros AM, Broadfield LA, Fendt S-M. Nutrient metabolism and cancer in the in vivo context: a metabolic game of give and take. EMBO Rep. 2020;21: e50635.

11. Gouirand V, Guillaumond F, Vasseur S. Influence of the tumor microenvironment on cancer cells metabolic reprogramming. Front Oncol. 2018;8. doi:10.3389/fonc.2018.00117

12. Lyssiotis CA, Kimmelman AC. Metabolic interactions in the tumor microenvironment. Trends Cell Biol. 2017;27: 863–875.

13. Muir A, Danai LV, Vander Heiden MG. Microenvironmental regulation of cancer cell metabolism: implications for experimental design and translational studies. Dis Model Mech. 2018;11. doi:10.1242/dmm.035758

14. Wiig H, Swartz MA. Interstitial fluid and lymph formation and transport: physiological regulation and roles in inflammation and cancer. Physiol Rev. 2012;92: 1005–1060.

15. Suvà ML, Tirosh I. Single-Cell RNA Sequencing in Cancer: Lessons Learned and Emerging Challenges. Mol Cell. 2019;75: 7–12.

16. Armingol E, Officer A, Harismendy O, Lewis NE. Deciphering cell-cell interactions and communication from gene expression. Nat Rev Genet. 2021;22: 71–88.

17. Naba A, Pearce OMT, Del Rosario A, Ma D, Ding H, Rajeeve V, et al. Characterization of the Extracellular Matrix of Normal and Diseased Tissues Using Proteomics. J Proteome Res. 2017;16: 3083–3091.

18. Infanger DW, Lynch ME, Fischbach C. Engineered culture models for studies of tumor-microenvironment interactions. Annu Rev Biomed Eng. 2013;15: 29–53.

19. Franco-Barraza J, Beacham DA, Amatangelo MD, Cukierman E. Preparation of Extracellular Matrices Produced by Cultured and Primary Fibroblasts. Curr Protoc Cell Biol. 2016;71: 10.9.1-10.9.34.

20. Wishart AL, Conner SJ, Guarin JR, Fatherree JP, Peng Y, McGinn RA, et al. Decellularized extracellular matrix scaffolds identify full-length collagen VI as a driver of breast cancer cell invasion in obesity and metastasis. Sci Adv. 2020;6. doi:10.1126/sciadv.abc3175

21. Elia I, Fendt S-M. In vivo cancer metabolism is defined by the nutrient microenvironment. Transl Cancer Res. 2016;5: S1284–S1287.

22. Garcia-Bermudez J, Williams RT, Guarecuco R, Birsoy K. Targeting extracellular nutrient dependencies of cancer cells. Mol Metab. 2020;33: 67–82.

23. Goel S, Duda DG, Xu L, Munn LL, Boucher Y, Fukumura D, et al. Normalization of the vasculature for treatment of cancer and other diseases. Physiol Rev. 2011;91: 1071–1121.

24. Olive KP, Jacobetz MA, Davidson CJ, Gopinathan A, McIntyre D, Honess D, et al. Inhibition of Hedgehog signaling enhances delivery of chemotherapy in a mouse model of pancreatic cancer. Science. 2009;324: 1457–1461.

25. Provenzano PP, Cuevas C, Chang AE, Goel VK, Von Hoff DD, Hingorani SR. Enzymatic targeting of the stroma ablates physical barriers to treatment of pancreatic ductal adenocarcinoma. Cancer Cell. 2012;21: 418–429.

26. Gullino PM, Clark SH, Grantham FH. The interstitial fluid of solid tumors. Cancer Res. 1964;24: 780–794.

27. Ho P-C, Bihuniak JD, Macintyre AN, Staron M, Liu X, Amezquita R, et al. Phosphoenolpyruvate Is a Metabolic Checkpoint of Anti-tumor T Cell Responses. Cell. 2015;162: 1217–1228.

28. Vecchio E, Caiazza C, Mimmi S, Avagliano A, Iaccino E, Brusco T, et al. Metabolites profiling of melanoma interstitial fluids reveals uridine diphosphate as potent immune modulator capable of limiting tumor growth. Front Cell Dev Biol. 2021;9: 730726.

29. Martínez-Reyes I, Chandel NS. Cancer metabolism: looking forward. Nat Rev Cancer. 2021;21: 669–680.

30. Reid MA, Kong M. Dealing with hunger: Metabolic stress responses in tumors. J Carcinog. 2013;12: 17.

31. Orth M, Metzger P, Gerum S, Mayerle J, Schneider G, Belka C, et al. Pancreatic ductal adenocarcinoma: biological hallmarks, current status, and future perspectives of combined modality treatment approaches. Radiat Oncol. 2019;14. doi:10.1186/s13014-019-1345-6

32. Cohen R, Neuzillet C, Tijeras-Raballand A, Faivre S, de Gramont A, Raymond E. Targeting cancer cell metabolism in pancreatic adenocarcinoma. Oncotarget. 2015;6: 16832–16847.

33. Ackermann T, Tardito S. Cell culture medium formulation and its implications in cancer metabolism. Trends Cancer. 2019;5: 329–332.

34. Cantor JR. The Rise of Physiologic Media. Trends Cell Biol. 2019;29: 854–861.

35. Haslene-Hox H. Measuring gradients in body fluids - A tool for elucidating physiological processes, diagnosis and treatment of disease. Clin Chim Acta. 2019;489: 233–241.

36. Wiig H, Tenstad O, Iversen PO, Kalluri R, Bjerkvig R. Interstitial fluid: the overlooked component of the tumor microenvironment? Fibrogenesis Tissue Repair. 2010;3: 12.

37. Haslene-Hox H, Oveland E, Berg KC, Kolmannskog O, Woie K, Salvesen HB, et al. A new method for isolation of interstitial fluid from human solid tumors applied to proteomic analysis of ovarian carcinoma tissue. PLoS One. 2011;6: e19217.

38. Wiig H, Berggreen E, Borge BAS, Iversen PO. Demonstration of altered signaling responses in bone marrow extracellular fluid during increased hematopoiesis in rats using a centrifugation method. Am J Physiol Heart Circ Physiol. 2004;286: H2028-34.

39. Wiig H, Aukland K, Tenstad O. Isolation of interstitial fluid from rat mammary tumors by a centrifugation method. Am J Physiol Heart Circ Physiol. 2003;284: H416-24.

40. Sullivan MR, Danai LV, Lewis CA, Chan SH, Gui DY, Kunchok T, et al. Quantification of microenvironmental metabolites in murine cancers reveals determinants of tumor nutrient availability. Elife. 2019;8. doi:10.7554/elife.44235

41. Apiz-Saab JJ, Dzierozynski LN, Jonker PB, Zhu Z, Chen RN, Oh M, et al. Pancreatic tumors activate arginine biosynthesis to adapt to myeloid-driven amino acid stress. bioRxiv. 2022. p. 2022.06.21.497008. doi:10.1101/2022.06.21.497008

42. Lee M-S, Dennis C, Naqvi I, Dailey L, Lorzadeh A, Ye G, et al. Ornithine aminotransferase supports polyamine synthesis in pancreatic cancer. Nature. 2023; 1–9.

43. Ngo B, Kim E, Osorio-Vasquez V, Doll S, Bustraan S, Liang RJ, et al. Limited Environmental Serine and Glycine Confer Brain Metastasis Sensitivity to PHGDH Inhibition. Cancer Discov. 2020 [cited 22 Jun 2020]. doi:10.1158/2159-8290.CD-19-1228

44. Ferraro GB, Ali A, Luengo A, Kodack DP, Deik A, Abbott KL, et al. Fatty acid synthesis is required for breast cancer brain metastasis. Nature Cancer. 2021; 1–15.

45. Sciacovelli M, Dugourd A, Jimenez LV, Yang M, Nikitopoulou E, Costa ASH, et al. Dynamic partitioning of branched-chain amino acids-derived nitrogen supports renal cancer progression. Nat Commun. 2022;13: 1–20.

46. Christen S, Lorendeau D, Schmieder R, Broekaert D, Metzger K, Veys K, et al. Breast Cancer-Derived Lung Metastases Show Increased Pyruvate Carboxylase-Dependent Anaplerosis. Cell Rep. 2016;17: 837–848.

47. Altea-Manzano P, Doglioni G, Liu Y, Cuadros AM, Nolan E, Fernández-García J, et al. A palmitate-rich metastatic niche enables metastasis growth via p65 acetylation resulting in pro-metastatic NF-κB signaling. Nature Cancer. 2023; 1–21.

48. Heintzman DR, Fisher EL, Rathmell JC. Microenvironmental influences on T cell immunity in cancer and inflammation. Cell Mol Immunol. 2022;19: 316–326.

49. Anderson KG, Stromnes IM, Greenberg PD. Obstacles Posed by the Tumor Microenvironment to T cell Activity: A Case for Synergistic Therapies. Cancer Cell. 2017;31: 311–325.

50. Zhang Y, Kurupati R, Liu L, Zhou XY, Zhang G, Hudaihed A, et al. Enhancing CD8+ T cell fatty acid catabolism within a metabolically challenging tumor microenvironment increases the efficacy of melanoma immunotherapy. Cancer Cell. 2017;32: 377-391.e9.

51. Reinfeld BI, Madden MZ, Wolf MM, Chytil A, Bader JE, Patterson AR, et al. Cell-programmed nutrient partitioning in the tumour microenvironment. Nature. 2021; 1–7.

52. Siska PJ, Beckermann KE, Mason FM, Andrejeva G, Greenplate AR, Sendor AB, et al. Mitochondrial dysregulation and glycolytic insufficiency functionally impair CD8 T cells infiltrating human renal cell carcinoma. JCI Insight. 2017;2. doi:10.1172/jci.insight.93411

53. Watson MJ, Vignali PDA, Mullett SJ, Overacre-Delgoffe AE, Peralta RM, Grebinoski S, et al. Metabolic support of tumour-infiltrating regulatory T cells by lactic acid. Nature. 2021. doi:10.1038/s41586-020-03045-2

54. Xu S, Chaudhary O, Rodríguez-Morales P, Sun X, Chen D, Zappasodi R, et al. Uptake of oxidized lipids by the scavenger receptor CD36 promotes lipid peroxidation and dysfunction in CD8+ T cells in tumors. Immunity. 2021. doi:10.1016/j.immuni.2021.05.003

55. Eil R, Vodnala SK, Clever D, Klebanoff CA, Sukumar M, Pan JH, et al. Ionic immune suppression within the tumour microenvironment limits T cell effector function. Nature. 2016;537: 539–543.

56. Quinn WJ, Jiao J, TeSlaa T, Stadanlick J, Wang Z, Wang L, et al. Lactate Limits T Cell Proliferation via the NAD(H) Redox State. Cell Rep. 2020;33. doi:10.1016/j.celrep.2020.108500

57. Vodnala SK, Eil R, Kishton RJ, Sukumar M, Yamamoto TN, Ha N-H, et al. T cell stemness and dysfunction in tumors are triggered by a common mechanism. Science. 2019;363. doi:10.1126/science.aau0135

58. Horvath P, Aulner N, Bickle M, Davies AM, Nery ED, Ebner D, et al. Screening out irrelevant cell-based models of disease. Nat Rev Drug Discov. 2016;15: 751–769.

59. Sullivan MR, Lewis CA, Muir A. Isolation and Quantification of Metabolite Levels in Murine Tumor Interstitial Fluid by LC/MS. Bio Protoc. 2019;9: e3427.

60. Li J, Byrne KT, Yan F, Yamazoe T, Chen Z, Baslan T, et al. Tumor Cell-Intrinsic Factors Underlie Heterogeneity of Immune Cell Infiltration and Response to Immunotherapy. Immunity. 2018;49: 178-193.e7.

61. Bechard ME, Smalling R, Hayashi A, Zhong Y, Word AE, Campbell SL, et al. Pancreatic cancers suppress negative feedback of glucose transport to reprogram chromatin for metastasis. Nat Commun. 2020;11: 4055.

62. Lien EC, Westermark AM, Zhang Y, Yuan C, Li Z, Lau AN, et al. Low glycaemic diets alter lipid metabolism to influence tumour growth. Nature. 2021;599: 302–307.

63. Hosios AM, Hecht VC, Danai LV, Johnson MO, Rathmell JC, Steinhauser ML, et al. Amino Acids Rather than Glucose Account for the Majority of Cell Mass in Proliferating Mammalian Cells. Dev Cell. 2016;36: 540–549.

64. Jain M, Nilsson R, Sharma S, Madhusudhan N, Kitami T, Souza AL, et al. Metabolite profiling identifies a key role for glycine in rapid cancer cell proliferation. Science. 2012;336: 1040–1044.

65. Muir A, Danai LV, Gui DY, Waingarten CY, Lewis CA, Vander Heiden MG. Environmental cystine drives glutamine anaplerosis and sensitizes cancer cells to glutaminase inhibition. Elife. 2017;6. doi:10.7554/eLife.27713

66. Afgan E, Baker D, Batut B, van den Beek M, Bouvier D, Cech M, et al. The Galaxy platform for accessible, reproducible and collaborative biomedical analyses: 2018 update. Nucleic Acids Res. 2018;46: W537–W544.

67. Dündar F, Skrabanek L, Zumbo P. Introduction to differential gene expression analysis using RNA-seq. Zenodo; 2015. doi:10.5281/ZENODO.3985047

68. Parekh S, Ziegenhain C, Vieth B, Enard W, Hellmann I. The impact of amplification on differential expression analyses by RNA-seq. Sci Rep. 2016;6: 25533.

69. Law CW, Chen Y, Shi W, Smyth GK. voom: Precision weights unlock linear model analysis tools for RNA-seq read counts. Genome Biol. 2014;15: R29.

70. Korotkevich G, Sukhov V, Budin N, Shpak B, Artyomov MN, Sergushichev A. Fast gene set enrichment analysis. bioRxiv. 2021. p. 060012. doi:10.1101/060012

71. Reich M, Liefeld T, Gould J, Lerner J, Tamayo P, Mesirov JP. GenePattern 2.0. Nat Genet. 2006;38: 500–501.

72. Subramanian A, Tamayo P, Mootha VK, Mukherjee S, Ebert BL, Gillette MA, et al. Gene set enrichment analysis: a knowledge-based approach for interpreting genome-wide expression profiles. Proc Natl Acad Sci U S A. 2005;102: 15545–15550.

73. Morris JP 4th, Yashinskie JJ, Koche R, Chandwani R, Tian S, Chen C-C, et al. α-Ketoglutarate links p53 to cell fate during tumour suppression. Nature. 2019;573: 595–599.

74. Lewis CA, Parker SJ, Fiske BP, McCloskey D, Gui DY, Green CR, et al. Tracing compartmentalized NADPH metabolism in the cytosol and mitochondria of mammalian cells. Mol Cell. 2014;55: 253–263.

75. Sanjana NE, Shalem O, Zhang F. Improved vectors and genome-wide libraries for CRISPR screening. Nat Methods. 2014;11: 783–784.

76. Shalem O, Sanjana NE, Hartenian E, Shi X, Scott DA, Mikkelson T, et al. Genome-scale CRISPR-Cas9 knockout screening in human cells. Science. 2014;343: 84–87.

77. Fellmann C, Hoffmann T, Sridhar V, Hopfgartner B, Muhar M, Roth M, et al. An optimized microRNA backbone for effective single-copy RNAi. Cell Rep. 2013;5: 1704–1713.

78. Erstad DJ, Sojoodi M, Taylor MS, Ghoshal S, Razavi AA, Graham-O'Regan KA, et al. Orthotopic and heterotopic murine models of pancreatic cancer and their different responses to FOLFIRINOX chemotherapy. Dis Model Mech. 2018;11. doi:10.1242/dmm.034793

79. Steggerda SM, Bennett MK, Chen J, Emberley E, Huang T, Janes JR, et al. Inhibition of arginase by CB-1158 blocks myeloid cell-mediated immune suppression in the tumor microenvironment. J Immunother Cancer. 2017;5: 101.

80. Lane AN, Yan J, Fan TW-M. 13C Tracer Studies of Metabolism in Mouse Tumor Xenografts. Bio Protoc. 2015;5. doi:10.21769/bioprotoc.1650

81. Millard P, Delépine B, Guionnet M, Heuillet M, Bellvert F, Létisse F. IsoCor: isotope correction for high-resolution MS labeling experiments. Bioinformatics. 2019;35: 4484–4487.

82. Pavlova NN, Thompson CB. The emerging hallmarks of cancer metabolism. Cell Metab. 2016;23: 27–47.

83. Muir A, Vander Heiden MG. The nutrient environment affects therapy. Science. 2018;360: 962–963.

84. Palm W, Thompson CB. Nutrient acquisition strategies of mammalian cells. Nature. 2017;546: 234–242.

85. Wellen KE, Thompson CB. Cellular metabolic stress: Considering how cells respond to nutrient excess. Mol Cell. 2010;40: 323–332.

86. Fukumura D, Duda DG, Munn LL, Jain RK. Tumor microvasculature and microenvironment: Novel insights through intravital imaging in pre-clinical models. Microcirculation. 2010;17: 206–225.

87. Vitale I, Manic G, Coussens LM, Kroemer G, Galluzzi L. Macrophages and metabolism in the tumor microenvironment. Cell Metab. 2019;30: 36–50.

88. Lonnroth P, Jansson PA, Smith U. A microdialysis method allowing characterization of intercellular water space in humans. Am J Physiol Endocrinol Metab. 1987;253: E228–E231.

89. Wibom C, Surowiec I, Mörén L, Bergström P, Johansson M, Antti H, et al. Metabolomic patterns in glioblastoma and changes during radiotherapy: a clinical microdialysis study. J Proteome Res. 2010;9: 2909–2919.

90. Cantor JR, Abu-Remaileh M, Kanarek N, Freinkman E, Gao X, Louissaint A Jr, et al. Physiologic Medium Rewires Cellular Metabolism and Reveals Uric Acid as an Endogenous Inhibitor of UMP Synthase. Cell. 2017;169: 258-272.e17.

91. Vande Voorde J, Ackermann T, Pfetzer N, Sumpton D, Mackay G, Kalna G, et al. Improving the metabolic fidelity of cancer models with a physiological cell culture medium. Sci Adv. 2019;5: eaau7314.

92. Bardeesy N, Aguirre AJ, Chu GC, Cheng K-H, Lopez LV, Hezel AF, et al. Both p16(Ink4a) and the p19(Arf)-p53 pathway constrain progression of pancreatic adenocarcinoma in the mouse. Proc Natl Acad Sci U S A. 2006;103: 5947–5952.

93. Michl J, Park KC, Swietach P. Evidence-based guidelines for controlling pH in mammalian live-cell culture systems. Commun Biol. 2019;2: 144.

94. Raghavan S, Winter PS, Navia AW, Williams HL, DenAdel A, Lowder KE, et al. Microenvironment drives cell state, plasticity, and drug response in pancreatic cancer. Cell. 2021;184: 6119-6137.e26.

95. Mootha VK, Lindgren CM, Eriksson K-F, Subramanian A, Sihag S, Lehar J, et al. PGC-1alpha-responsive genes involved in oxidative phosphorylation are coordinately downregulated in human diabetes. Nat Genet. 2003;34: 267–273.

96. Chisolm DA, Weinmann AS. Connections between metabolism and epigenetics in programming cellular differentiation. Annu Rev Immunol. 2018;36: 221–246.

97. Dai Z, Ramesh V, Locasale JW. The evolving metabolic landscape of chromatin biology and epigenetics. Nat Rev Genet. 2020;21: 737–753.

98. Diehl KL, Muir TW. Chromatin as a key consumer in the metabolite economy. Nat Chem Biol. 2020;16: 620–629.

99. Reid MA, Dai Z, Locasale JW. The impact of cellular metabolism on chromatin dynamics and epigenetics. Nat Cell Biol. 2017;19: 1298–1306.

100. Jensen C, Teng Y. Is it time to start transitioning from 2D to 3D cell culture? Front Mol Biosci. 2020;7: 33.

101. Pampaloni F, Reynaud EG, Stelzer EHK. The third dimension bridges the gap between cell culture and live tissue. Nat Rev Mol Cell Biol. 2007;8: 839–845.

102. Metcalf KJ, Alazzeh A, Werb Z, Weaver VM. Leveraging microenvironmental synthetic lethalities to treat cancer. J Clin Invest. 2021;131. doi:10.1172/JCI143765

103. Sela Y, Li J, Maheswaran S, Norgard R, Yuan S, Hubbi M, et al. Bcl-xL enforces a slow-cycling state necessary for survival in the nutrient-deprived microenvironment of pancreatic cancer. Cancer Res. 2022;82: 1890–1908.

104. Haines RJ, Pendleton LC, Eichler DC. Argininosuccinate synthase: at the center of arginine metabolism. Int J Biochem Mol Biol. 2011;2: 8–23.

105. Garcia-Bermudez J, Baudrier L, La K, Zhu XG, Fidelin J, Sviderskiy VO, et al. Aspartate is a limiting metabolite for cancer cell proliferation under hypoxia and in tumours. Nat Cell Biol. 2018;20: 775–781.

106. Sullivan LB, Luengo A, Danai LV, Bush LN, Diehl FF, Hosios AM, et al. Aspartate is an endogenous metabolic limitation for tumour growth. Nat Cell Biol. 2018;20: 782–788.

107. Rabinovich S, Adler L, Yizhak K, Sarver A, Silberman A, Agron S, et al. Diversion of aspartate in ASS1-deficient tumours fosters de novo pyrimidine synthesis. Nature. 2015;527: 379–383.

108. Lee JS, Adler L, Karathia H, Carmel N, Rabinovich S, Auslander N, et al. Urea cycle dysregulation generates clinically relevant genomic and biochemical signatures. Cell. 2018;174: 1559-1570.e22.

109. Albaugh VL, Pinzon-Guzman C, Barbul A. Arginine-Dual roles as an onconutrient and immunonutrient. Journal of Surgical Oncology. 2017. pp. 273–280. doi:10.1002/jso.24490

110. Closs EI, Simon A, Vékony N, Rotmann A. Plasma membrane transporters for arginine. J Nutr. 2004;134: 2752S-2759S; discussion 2765S-2767S.

111. Gong H, Zölzer F, von Recklinghausen G, Havers W, Schweigerer L. Arginine deiminase inhibits proliferation of human leukemia cells more potently than asparaginase by inducing cell cycle arrest and apoptosis. Leukemia. 2000;14: 826–829.

112. Changou CA, Chen Y-R, Xing L, Yen Y, Chuang FYS, Cheng RH, et al. Arginine starvation-associated atypical cellular death involves mitochondrial dysfunction, nuclear DNA leakage, and chromatin autophagy. Proc Natl Acad Sci U S A. 2014;111: 14147–14152.

113. Chantranupong L, Scaria SM, Saxton RA, Gygi MP, Shen K, Wyant GA, et al. The CASTOR proteins are arginine sensors for the mTORC1 pathway. Cell. 2016;165: 153–164.

114. Albaugh VL, Barbul A. Arginine. Reference Module in Life Sciences. 2017. doi:10.1016/b978-0-12-809633-8.06082-9

115. Zaytouni T, Tsai P-Y, Hitchcock DS, DuBois CD, Freinkman E, Lin L, et al. Critical role for arginase 2 in obesity-associated pancreatic cancer. Nat Commun. 2017;8: 242.

116. Grima-Reyes M, Martinez-Turtos A, Abramovich I, Gottlieb E, Chiche J, Ricci J-E. Physiological impact of in vivo stable isotope tracing on cancer metabolism. Molecular Metabolism. 2021;53: 101294.

117. Boelens PG, van Leeuwen PAM, Dejong CHC, Deutz NEP. Intestinal renal metabolism of L-citrulline and L-arginine following enteral or parenteral infusion of L-alanyl-L-[2,15N]glutamine or L-[2,15N]glutamine in mice. Am J Physiol Gastrointest Liver Physiol. 2005;289: G679-85.

118. Buescher JM, Antoniewicz MR, Boros LG, Burgess SC, Brunengraber H, Clish CB, et al. A roadmap for interpreting 13C metabolite labeling patterns from cells. Curr Opin Biotechnol. 2015;34: 189–201.

119. Rogers LC, Van Tine BA. Innate and adaptive resistance mechanisms to arginine deprivation therapies in sarcoma and other cancers. Canc Drug Resist. 2019;2: 516–526.

120. Rogers LC, Zhou J, Baker A, Schutt CR, Panda PK, Van Tine BA. Intracellular arginine-dependent translation sensor reveals the dynamics of arginine starvation response and resistance in ASS1-negative cells. Cancer Metab. 2021;9: 4.

121. Crump NT, Hadjinicolaou AV, Xia M, Walsby-Tickle J, Gileadi U, Chen J-L, et al. Chromatin accessibility governs the differential response of cancer and T cells to arginine starvation. Cell Rep. 2021;35: 109101.

122. Palm W. Metabolic functions of macropinocytosis. Philos Trans R Soc Lond B Biol Sci. 2019;374: 20180285.

123. Commisso C, Davidson SM, Soydaner-Azeloglu RG, Parker SJ, Kamphorst JJ, Hackett S, et al. Macropinocytosis of protein is an amino acid supply route in Ras-transformed cells. Nature. 2013;497: 633–637.

124. Yao W, Rose JL, Wang W, Seth S, Jiang H, Taguchi A, et al. Syndecan 1 is a critical mediator of macropinocytosis in pancreatic cancer. Nature. 2019;568: 410–414.

125. Yu T, Lin L, Wen K, Xing L, Liu J, Cho S-F, et al. Syndecan-1 Is Critical in ARF6-Dependent Macropinocytosis Driven By KRAS Mutation in the Pathophysiology of Multiple Myeloma. Blood. 2019;134: 4371–4371.

126. Hajaj E, Sciacovelli M, Frezza C, Erez A. The context-specific roles of urea cycle enzymes in tumorigenesis. Mol Cell. 2021;81: 3749–3759.

127. Kamphorst JJ, Nofal M, Commisso C, Hackett SR, Lu W, Grabocka E, et al. Human pancreatic cancer tumors are nutrient poor and tumor cells actively scavenge extracellular protein. Cancer Res. 2015;75: 544–553.

128. Palm W, Park Y, Wright K, Pavlova NN, Tuveson DA, Thompson CB. The Utilization of Extracellular Proteins as Nutrients Is Suppressed by mTORC1. Cell. 2015;162: 259–270.

129. Garcia-Bermudez J, Badgley MA, Prasad S, Baudrier L, Liu Y, La K, et al. Adaptive stimulation of macropinocytosis overcomes aspartate limitation in cancer cells under hypoxia. Nat Metab. 2022;4: 724–738.

130. Monterisi S, Michl J, Hulikova A, Koth J, Bridges EM, Hill AE, et al. Solute exchange through gap junctions lessens the adverse effects of inactivating mutations in metabolite-handling genes. Elife. 2022;11. doi:10.7554/eLife.78425

131. Francescone R, Barbosa Vendramini-Costa D, Franco-Barraza J, Wagner J, Muir A, Lau AN, et al. Netrin G1 Promotes Pancreatic Tumorigenesis through Cancer-Associated Fibroblast-Driven Nutritional Support and Immunosuppression. Cancer Discov. 2021;11: 446–479.

132. Lee JJ, Bernard V, Semaan A, Monberg ME, Huang J, Stephens BM, et al. Elucidation of tumor-stromal heterogeneity and the ligand-receptor interactome by single-cell transcriptomics in real-world pancreatic cancer biopsies. Clin Cancer Res. 2021;27: 5912–5921.

133. Zhu Y, Herndon JM, Sojka DK, Kim K-W, Knolhoff BL, Zuo C, et al. Tissue-resident macrophages in pancreatic ductal adenocarcinoma originate from embryonic hematopoiesis and promote tumor progression. Immunity. 2017;47: 597.

134. Trovato R, Fiore A, Sartori S, Canè S, Giugno R, Cascione L, et al. Immunosuppression by monocytic myeloid-derived suppressor cells in patients with pancreatic ductal carcinoma is orchestrated by STAT3. J Immunother Cancer. 2019;7: 255.

135. Sherman MH, Yu RT, Tseng TW, Sousa CM, Liu S, Truitt ML, et al. Stromal cues regulate the pancreatic cancer epigenome and metabolome. Proc Natl Acad Sci U S A. 2017;114: 1129–1134.

136. Sousa CM, Biancur DE, Wang X, Halbrook CJ, Sherman MH, Zhang L, et al. Pancreatic stellate cells support tumour metabolism through autophagic alanine secretion. Nature. 2016;536: 479–483.

137. Auciello FR, Bulusu V, Oon C, Tait-Mulder J, Berry M, Bhattacharyya S, et al. A stromal lysolipid-autotaxin signaling axis promotes pancreatic tumor progression. Cancer Discov. 2019;9: 617–627.

138. Caldwell RW, Rodriguez PC, Toque HA, Narayanan SP, Caldwell RB. Arginase: A multifaceted enzyme important in health and disease. Physiol Rev. 2018;98: 641–665.

139. Clausen BE, Burkhardt C, Reith W, Renkawitz R, Förster I. Conditional gene targeting in macrophages and granulocytes using LysMcre mice. Transgenic Res. 1999;8: 265–277.

140. El Kasmi KC, Qualls JE, Pesce JT, Smith AM, Thompson RW, Henao-Tamayo M, et al. Toll-like receptor-induced arginase 1 in macrophages thwarts effective immunity against intracellular pathogens. Nat Immunol. 2008;9: 1399–1406.

141. Menjivar RE, Nwosu ZC, Du W, Donahue KL, Hong HS, Espinoza C, et al. Arginase 1 is a key driver of immune suppression in pancreatic cancer. Elife. 2023;12. doi:10.7554/eLife.80721

142. Banh RS, Biancur DE, Yamamoto K, Sohn ASW, Walters B, Kuljanin M, et al. Neurons release Serine to support mRNA translation in pancreatic cancer. Cell. 2020;183: 1202-1218.e25.

143. Siegel RL, Miller KD, Jemal A. Cancer statistics, 2018. CA Cancer J Clin. 2018;68: 7–30.

144. Yamasaki A, Yanai K, Onishi H. Hypoxia and pancreatic ductal adenocarcinoma. Cancer Lett. 2020;484: 9–15.

145. Koong AC, Mehta VK, Le QT, Fisher GA, Terris DJ, Brown JM, et al. Pancreatic tumors show high levels of hypoxia. Int J Radiat Oncol Biol Phys. 2000;48: 919–922.

146. Li H, Fan X, Houghton J. Tumor microenvironment: the role of the tumor stroma in cancer. J Cell Biochem. 2007;101: 805–815.

147. Marcucci F, Bellone M, Caserta CA, Corti A. Pushing tumor cells towards a malignant phenotype: stimuli from the microenvironment, intercellular communications and alternative roads. Int J Cancer. 2014;135: 1265–1276.

148. Ugel S, Canè S, De Sanctis F, Bronte V. Monocytes in the Tumor Microenvironment. Annu Rev Pathol. 2021;16: 93–122.

149. DeNardo DG, Ruffell B. Macrophages as regulators of tumour immunity and immunotherapy. Nat Rev Immunol. 2019;19: 369–382.

150. Sahai E, Astsaturov I, Cukierman E, DeNardo DG, Egeblad M, Evans RM, et al. A framework for advancing our understanding of cancer-associated fibroblasts. Nat Rev Cancer. 2020;20: 174–186.

151. Fiedler EC, Hemann MT. Aiding and Abetting: How the Tumor Microenvironment Protects Cancer from Chemotherapy. Annu Rev Cancer Biol. 2019;3: 409–428.

152. Hirata E, Sahai E. Tumor Microenvironment and Differential Responses to Therapy. Cold Spring Harb Perspect Med. 2017;7. doi:10.1101/cshperspect.a026781

153. Quail DF, Joyce JA. Microenvironmental regulation of tumor progression and metastasis. Nat Med. 2013;19: 1423–1437.

154. Lorusso G, Rüegg C. The tumor microenvironment and its contribution to tumor evolution toward metastasis. Histochem Cell Biol. 2008;130: 1091–1103.

155. Pathria P, Louis TL, Varner JA. Targeting tumor-associated macrophages in cancer. Trends Immunol. 2019;40: 310–327.

156. Crespo J, Sun H, Welling TH, Tian Z, Zou W. T cell anergy, exhaustion, senescence, and stemness in the tumor microenvironment. Curr Opin Immunol. 2013;25: 214–221.

157. Geiger R, Rieckmann JC, Wolf T, Basso C, Feng Y, Fuhrer T, et al. L-Arginine Modulates T Cell Metabolism and Enhances Survival and Anti-tumor Activity. Cell. 2016;167: 829-842.e13.

158. Murray PJ. Amino acid auxotrophy as a system of immunological control nodes. Nat Immunol. 2016;17: 132–139.

159. Canale FP, Basso C, Antonini G, Perotti M, Li N, Sokolovska A, et al. Metabolic modulation of tumours with engineered bacteria for immunotherapy. Nature. 2021;598: 662–666.

160. Miret JJ, Kirschmeier P, Koyama S, Zhu M, Li YY, Naito Y, et al. Suppression of myeloid cell arginase activity leads to therapeutic response in a NSCLC mouse model by activating anti-tumor immunity. J Immunother Cancer. 2019;7: 32.

161. Sosnowska A, Chlebowska-Tuz J, Matryba P, Pilch Z, Greig A, Wolny A, et al. Inhibition of arginase modulates T-cell response in the tumor microenvironment of lung carcinoma. Oncoimmunology. 2021;10: 1956143.

162. Hilmi M, Bartholin L, Neuzillet C. Immune therapies in pancreatic ductal adenocarcinoma: Where are we now? World J Gastroenterol. 2018;24: 2137–2151.

163. Canè S, Barouni RM, Fabbi M, Cuozzo J, Fracasso G, Adamo A, et al. Neutralization of NET-associated human ARG1 enhances cancer immunotherapy. Sci Transl Med. 2023;15: eabq6221.